FINAL REPORT

EXPERIMENT ON S57 (later OSO III) Satellite (Cosmic Ray Charge and Energy Spectra)

Prepared by MORTON F KAPLON

National Aeronautics and Space Administration
Contract NAS 5-3178
(Including Subcontract Ball Brothers NAS 5-3178 S1)

June 1971

The University of Rochester

Department of Physics and Astronomy

Rochester, New York

I. Experiment Objectives

Our original objectives in formulating the proposal for the University of Rochester (UR) experiment on the S-57 (later OSO-III) satellite were an elucidation of the details of the high energy charged component in an environment free of the disadvantages accompanying such studies at balloon altitudes where the beam incident on the detector has been distorted by the overlying atmosphere.

These objectives were stated originally as a study of the following physical quantities.

(1) The charge composition of the quiescent cosmic radiation, the resolution being into charge groups specified as:

$Z = 1$	Consisting chiefly of protons
$Z = 2$	He Nuclei
$3 \leq Z \leq 5$	Designated as the L-group and consisting of Li, Be and B nuclei.
$6 \leq Z \leq 9$	Designated as the M-group and consisting of C, N, O and F nuclei.
$Z \geq 10$	Designated as the H-group and consisting of all nuclei of charge equal to or greater than 10.

(2) The integral energy spectrum of the five charge groups in (1), to be obtained by analysis of the data based on the one latitude effect (geomagnetic selection).

(3) The charge composition of solar flare emitted beams within the above resolution: (such observation was considered unlikely due to the relatively high energy imposed by instrumental cut-off as well as by the fact that the original launch schedule was at

solar minimum)

(4) The cosmic ray albedo, both of the splash and re-entrant type.

(5) Any modulation of the intensities as a function of time (realistically considered feasible only for P (roton) and the He nuclei for statistical reasons).

To these original objectives was added later, the following additional objective.

(6) The detection of high energy ($\gtrsim 50$ Mev) γ-rays of celestial origin.

II. Detector Design and Operation

In considering the detector design one must bear in mind several things relevant to the time of proposal. The most important of those technically was the extremely limited data handling capacity of the original OSO's coupled with the relative nascent state of large dynamic range, low power, pulse height analyzers. Of these, the former was dominant. Since the orbit was planned to be circular and to lie roughly between $\pm 30^{\circ}$ latitude, the a priori at expectation was the most of the charged particles would be relativistic. Given the requirement of charge separation for relativistic particles the most natural detector is a Cerenkov radiator since for a given velocity its response is directly proportional to Z^2 and its directional properties insure that one knows the orientation of particles passing through it. Those basic considerations led to the selection of a Cerenkov detector as the basic element of the telescope. Other elements were added, of course, to define the geometry and to assist in defining as well as possible the nature of particles passing through the instrument.

With all of these considerations folded in and the space limitations of the compartment taken into account, the final instrument configuration in schematic outline is shown in Fig. 1. The elements labeled X, A, C and D are plastic scintillators, A and X being 1/4" thick, C being 1/2" thick and D approximately a hollowed-cut cylinder, B is a lucite Cerenkov radiator 1" thick, blackened at the top to insure a unidirectional sensitivity. Beneath A was inserted a 1/16" thick Pb disc to serve as a converter of high energy γ-rays to electron-positron pairs for the detection of γ-rays. For charged particles the geometry is basically defined by the A and C counters. The B-sleeve is employed in anti-coincidence to prevent false counts due to knock-on particles and from showers produced by high energy interactions. The X scintillator is used for further discrimination against charged particles in the γ-ray mode. The Cerenkov counter B was the prime source of information about particles passing through and a signal from it gave assurance with a relatively high degree of confidence (95%) that the passage of a particle was in the direction $A \rightarrow B \rightarrow C$.

In considering the instrument, one of the first factors to assess is its geometrical response. Fig. 2 portrays the results of a Monte Carlo calculation on variation of the differential solid angle ($A\Omega$) as a function of the angle the particle makes with the telescope axis It is clear from this that most of the particles accepted for either the logic AC or $AC\bar{D}$ make angles 15° with the axis. This is illustrated more quantitatively in Fig. 3 where the efficiency as a function of angle with the telescope axis is presented for both logic requirements AC and $AC\bar{D}$ · 15° is the midpoint of the fall off from the uniform value. The actual value of the geometrical factor for an isotropic flux incident on the detector from these calculations is $(A\Omega)_{AC} = 2.77\ cm^2 ster$ and $(A\Omega)_{AC\bar{D}} = 2.29\ cm^2 ster$.

The effective limitation to angles less than 15° is of importance since it assures that any signal broadening due to purely geometric traversal effects will be less than $1/\cos 15^{\circ} = 1.035$, an insignificant factor compared to other effects. The logic decided upon for data acquistion was as follows. For observations on protons and He nuclei the coincidence $AB_{ij}C\bar{D}$; for nuclei of $Z \geq 2$ the coincidence $A'B_{ij}C'$; and for γ-rays $\overline{XA}B_{\gamma_1\gamma_2}C\bar{D}$. Here A and A', C and C' represent for both detectors A and C, lower level thresholds, with the ' level significantly higher than the unprimed level. B_{ij} and $B_{\gamma_1\gamma_2}$ represents a series of preset differential bands of the light output from the Cerenkov detector B and the ‾ over the letter indicates as usual an anti-coincidence.

We will discuss first the B-detector. As noted earlier, the limited data transmission capability of the original OSO series and the state of the art of wide dynamic range pulse height analyzers imposed a restricted mode of handling the data in which we decided to analyze our signals using preset discriminator levels and the assumption that all particles would be relativistic. Since we were using preset discriminators for signal processing, it was clearly desirable to have a check on the system response and this was realized by running the detector in two operational modes, denoted as I and II. I is the actual data gathering mode and II (actuated every 16th orbit) is a calibration mode to check the stability and response of the system.

The Cerenkov detector B has a light output given by $dN_\gamma/dl = KZ^2(1-\frac{1}{n^2\beta^2})$, where dN_γ/dl is the number of photons in a given spectral band, K a constant depending on the band, n the index of refraction (=1.5 for lucite) and β the velocity in units of c . dN_γ/dl is plotted (in arbitrary units) for lucite in Fig. 4 versus the kinetic energy/nucleon expressed in units of mc^2; $\gamma-1 = (1-\beta^2)^{-1/2} -1$. Our assumption was that γ-1 for primary particles for essentially the entire orbit would fall within the asymptotically flat response region corresponding to $\beta = 1$. We will thus take as unit signal height in the 1 inch Cerenkov detector the value of 1 for a Z = 1, $\beta = 1$ particle traversing it normally. Thus, the signal expected for a particle of charge Z is $S(Z, \beta=1) = Z^2 S(Z=1,\beta=1) = Z^2$ in the units adopted. The actual signal observed will not be, for a fixed type of particle at a fixed velocity, a single fixed value due to fluctuations arising from the photon conversion in the photomultiplier (PM) cathode.

for the types of cathodes (S-11) and conversion efficiences (~10%) available at the time we expected to obtain resolution for $\beta=1$, $Z=1$ particles of about 50% FWHM (fullwidth at half maximum). A significant part of our effort was based on obtaining this response experimentally for the B -P.M. tubes to be used since all of our electronic thresholds had to be set on this basis.

Thus, sea level μ-mesons were used for basic calibration of the Cerenkov response since they comprise a beam (albeit of low intensity) of $\beta=1$, $Z=1$ particles. A typical B response as observed in the actual detector geometry is portrayed in Fig. 5. (A 400 channel RIDL analyzer gated by $AC\bar{D}$ was used.) It should be noted that this response contains an overaging over the detector geometry (with a $\cos^2\theta$ incident flux rather than isotropic, the difference, however, being negligible) as well as the P.M. overall response. The histogram in the figure represents the way the same distribution would be read out in the preset differential bins of the calibration mode (II) which were set as (in our units of the maximum value=1):

i	j	Bin Label
0.25	0.55	P_1
0.55	0.85	P_2
0.85	1.15	P_3
1.15	1.45	P_4
1.45	1.75	P_5
1.75	2.6	P_6

Using the observed B-signal distribution for $\beta=1$, Z=1 particles, the expected distributions for the other values of Z were calculated by an appropriate scaling of the μ-meson response. Fig. 6 represents the calculation for the He (Z=2) and Li (Z=3) response based on the observed μ-meson response. The resolution as a function of Z is FWHM (Z)=1/Z FWHM (Z=1). Indicated also on Fig. 6 are the thresholds for the discriminators which define the Mode II differential bands, P_1-P_6, the band defining He-nuclei (2.6-6.8) and the band defining L-nuclei (7.0-32). The discriminator settings were determined utilizing the distributions and the a priori expectation that the relative intensities $I^{(P)}/I^{(He)} \approx 7$ and $I^{(He)}/I^{(L)} \approx 50$. The latter high ratio indicated the desirability of the gap between the upper end of He and the lower end of the L-nuclei band.

Fig. 7 shows the calculated pulse height distributions (normalized to $\beta=1$, Z=1 peak at 1) for Z=2,3,5,6,9, and 10 nuclei and the normalized discriminator thresholds defining the differential bands, B_{ij} of P(rotons), He, L, M and H nuclei. Figures 8 and 9 give typical responses to μ-mesons of the A and C scintillators respectively, with the calculated responses to Z=3 nuclei; indicated by A, A' and C, C' are the discriminator thresholds for the recording it logic signals from these elements. Fig. 10 gives the observed response of the X scintillator to μ-mesons and the setting of its discriminator level for use in the logic. Due to the lack of symmetry the D-anticoincidence scintillator presents to an isotropic beam and to the large variations in path length of particles traversing it, any pulse height distribution of it (D) has essentially no meaning.

The discriminator level settings were determined here using external probe counters to check the passage of μ-mesons through short path areas, utilization of expected singles counting rates and the ration of geometrical factors calculated being in agreement with observation on μ-mesons.

Details of materials used, optical coupling procedures, etc , are contained in the BBRC Final Report, Section 2, pgs. 2-1 to 2-11

As noted earlier the digital data to be recorded for charged particles is represented by the logic AC, $AC\overline{D}$, $AB_{ij}C\overline{D}$ and $A'B_{ij}C'$ The levels B_{ij} in the mode accompanying $AC\overline{D}$ are indicated in Figs. 6 and 7 and the A and C levels in Figs. 8 and 9. For detection of nuclei of $Z > 2$ the D anti-coincidence had to be dropped as a balloon test flight confirmed our expectation that fast knock-on electrons would trigger the D sufficiently to veto most of the $Z > 2$ particles. The levels of A' and C' were set as indicated in Figs. 8 and 9 to require the passage of a particle of charge 3 through A and C in order to gain some tightening of trigger requirements to compensate for the loss of the D-anti-coincidence. The levels for B_{ij} are indicated on Figs. 6 and 7. The calbration mode thresholds are indicated also in Figs 5 and 6 where the differential bins P_1-P_6 are indicated.

The γ-ray channel consists of the logic $\overline{XA}B_{\gamma_1\gamma_2}C\overline{D}$. The A and C thresholds are those indicated in Figs 8 and 9 and the X threshold is that shown in Fig 10 For $B_{\gamma_1\gamma_2}$, $\gamma_1 = 1.15$ and $\gamma_2 = 6.8$ and is indicated also in Fig 6 The overall efficiency of the $\overline{XA}$ anti-coincidence was estimated several ways. One way was to put the entire detector under 20 cm of Pb (to reduce the finite but small sea level γ-ray flux) and to compare the γ-ray rate with the $P(AB_p\overline{CD})$ rate. (Fig. 11) This should give an upper limit due to μ-meson bremsstrahlung and gave a ratio of $\overline{XA}B_{\gamma_1\gamma_2}\overline{CD}/AB_p\overline{CD}=(2.1 \pm .5)\times10^{-3}$ Other methods involved using an external counter (E_1) and monitoring $E_1B_p\overline{CD}$ and $E_1XB_p\overline{CD}$, $E_1AB_p\overline{CD}$ to obtain firing efficiencies of the discriminators These all indicated $\overline{XA}$ rejection rates of 10^{-3}. The other important factor is the response to γ-rays as a function of energy This was studied in detail both theoretically, using Monte Carlo calculations, and experimentally, using the tagged γ-ray beam of the Cornell electron synchrotron. These results are covered in detail in Ref. 1 (Dennis and Share).

Table I is a listing of a summary of a set of counting rates for the instrument at a sea level exposure at Rochester for various orientations.

In addition to the digital data indicated in the proceeding, we had two analogue channels of data reception These were the anode current from the D-photomultipliers and the singles counting rate from the X-scintillator. Typical calibration runs are shown in Fig 12.

III Data Format

For a given mode of operations (Mode I = data mode, Mode II = calibration mode) the counts in the various logic channels were sorted into six sectors with respect to the observatory sun line utilizing a set of solar eyes on the wheel rim panel. Each sector was "live" for 40° with a "dead" sector 20° wide between each "live" sector; thus, the detector recorded 2/3 of the time per wheel revolution as a band in the wheel plane was swept out. For each sector, data was recorded in one main frame telemetry word and is accumulated over a period corresponding to eight main telemetry frames. Since one main frame corresponds to 32 words and requires 0.64 seconds to cycle and each of our sectors is read out sequentially over a cycle of eight, the live time per readout was 0.568 seconds. The other two words readout over the cycle corresponded to AC and $A\bar{\bar{C}}\bar{D}$ rates routed into sector 1 (solar sector) and sector 3. The two analogue channels for the X-count rate and D-anode currents were readout on the main frame subcommutator. Phototube power was on continuously but electronics power and data acquisition was available only for the daylight portions of the orbit. Details are servatory aspect is essentially constant and is so treated. For each type of data, the total number of main frame words analyzed is kept, so that the "look time" is accurately known and thus fluxes can be calculated.

The OSO-III traversed the artifical radiation belts, particularly at the South Atlantic anomaly, where all counting rates increased markedly. The effects of this are indicated for two passes, #179 and #324 in Figs. 15 and 16. In the former both the X-count rate and D-anode current monitors have saturated and the AC and AC$\bar{D}$ rates have saturated while the other rates have reached unphysical values, clearly reflecting the influence of the high radiation environment. In Fig. 16, where the count rate and anode current are around their ground test values (see Fig. 12) the data clearly is both different than in Fig. 15 and also cleaner. It was thus necessary to impose some constraints on the data acceptable for analysis and we accepted for analysis only that data for which the X-count rate and A-anode current monitors were each less than 40% above their maximum quiescent values (these monitors vary with geomagnetic latitude). In addition to the deletion of data on the above basis, we also edited out data flagged by synch bit errors and data identified as transmission errors according to internal logic criteria. One of those in fact resulted from the failure of the sector gate to sector 2 which occurred just after launch. This gate did not work and sector 2 was thus continuously live; it thus recorded the sum of counts in given in the BBRC report, Section 3, pgs. 3-1 to 3-18, Section 4, pgs. 4-7 to 4-11 and Section 6, pgs. 6-1 to 6-8. The checkout console is described in Section 6, pgs. 6-9 to 6-16.

IV. Balloon Flight Results

As part of our program of study we had proposed a rather extensive series of balloon flights of the engineering prototype to assist us in assessing performance and up-grading design. Only one successful flight was obtained, there being several balloon failures at the tropopause and finally the instrument package was lost after a balloon failure

In the balloon flights we were able to monitor more data channels than possible in the satellite format. The specifics of the flight are given in Table II-1, II-2 and Figs 13 and 14. Of particular note in Table II-2 is the comparison of the rates of the L, M and H channels with and without the requirement $\overline{D}$, indicating clearly the effect of $\overline{D}$ in cutting down the rates due to knock on electrons. The sensitivity of the P and α channels to the $\overline{D}$ requirement is also clearly reflected in this data as is the calibration data to the $\overline{D}$ requirement.

V. Data Analysis

A-General

The incoming data, in the various logic channels and sectors was summed over one minute intervals (e.g. a given signal logic in a given sector) of observatory time during which interval the obsectors 1,3,4,5,6 and 2 and this was used as an internal logic criteria on the data.

After the summation of the data over the basic time intervals and the deletion of data according to the above criteria, it is further sorted with respect to the zenith angle of the detector axis (ZA) and also with respect to magnetic rigidity. This sorted data is summed over 100 orbits as an initial summation, further summed over 700 orbit units, and finally the 700 orbit units are summed for a total data summation.

Some comments are clearly in order about the justification for summing our data over such long intervals of time. One is, of coarse, to obtain higher statistical accuracy, but that is only justified if there is a basis for assuming that the input is essentially constant over the period involved.

Fig. 17 shows a plot of the Dallas Neutron Monitor data (obtained from ESSA - SOLAR and GEOPHYSICAL DATA) in which it has been summed in such a way as to correspond approximately to our summation over 100 orbit intervals, in Fig. 17 these means are plotted against orbit number. Though there is an indication of a decrease with increasing orbit number (time), its magnitude is quite small. The largest fluctuation from the mean is 2.8%, while most fluctuations are about 1%, so that the variations are not large. The mean for the first 28 orbit period is 6120 and for the second 28 orbit period is 6070 so that the average variation is less than 1% over periods of about 6 months.

It is nevertheless worth looking at the time (orbit) variation of our data. We used the data summed over 100 orbit periods in order to have meaningful statistics and have examined the AC, $AC\bar{D}$ and P(roton) ($AB_P C\bar{D}$) channels for a variety of sorts of the data. The data is presented in Figs. 18, 19, 20 and 21. In Fig. 18 the data is selected in the zenith angle range 0-60° and corresponding to a vertical geomagnetic cutoff between 3.0 - 4.3 Bv. In Fig. 19 the zenith angle range is also 0-60° but the vertical cutoff corresponds to 12.5 - 15.0 Bv. Figs. 20 and 21 represent the zenith angle range 120-180° and respectively data corresponding to a vertical geomagnetic cutoff of 3.0 - 4.3 Bv and 12.5 - 15.0 Bv. The data presented in these figures has been subjected to the editing referred to previously.

Several comments should be made first. While typical statistical errors are indicated, for each channel there are some points with larger errors. For the vertical (0-60°) data (Figs. 18 and 19) there appear significant upward deviations at orbit numbers (in units of 100) 32.5, and 33.5 for the AC and $AC\bar{D}$ channels but none in the P-channel for the two extreme rigidity ranges, and an additional deviation at orbit number 34.5 for the high rigidity data that is not reflected at all in the low rigidity data for these two channels With respect to the albedo channels, while data is missing for orbit number 32.5, there is no indication at all of any significant deviation at orbit numbers 33.5 and 34.5.

In looking at this data one has to ask -- do the deviations from the mean (excluding the anomalous ones) represent just statistical fluctuations, instrumental vagaries, or are they more significant?

Let us consider first instrumental vagaries. This is, of course, a difficult question to answer with certainty, but we have no evidence in our assessment of any malfunction of the instrument In fact, the absence of the significant deviation at orbits 33-35 in the albedo channels of AC and AC$\overline{D}$ that appeared in those channels in the 0-60^{o} data argues fairly strongly against instrumental malfunction in the sensor end of the instrument as well as in the data handling and since the sorting is done in the analysis end and comes from data assembled continuously for several weeks. (The reason for zero data in the albedo direction for orbits 31-33 is a combination of geometry and the fact that the AC and AC$\overline{D}$ channels utilize only 2 of the 6 sectors with respect to the sun while the proton channel utilizes them all). We can thus find no substantive basis internally to argue for instrument misbehavior, rather the evidence argues against this.

We next turn to the question of statistical fluctuations. This, of course, only has meaning with respect to a test against some hypothesis and even there it only says (at best) that it is compatible (or not) with that hypothesis within certain confidence limits. The hypothesis that is suggested by experience and by looking at the data itself is to look for some periodic phenomena. We have done this, subjecting the data represented in Figs. 17-21 to a Fourier Power Spectrum Analysis using the Cooley-Tukey algorithm. The data of Fig. 17, i e. the Dallas neutron monitor was used as a check since there exists the well-known synodic solar rotation variation of the neutron monitor response The data was sorted in two ways One sort subjected the daily averages to the analysis and the other sort subjected the lumped averages (i.e of Fig. 17) to the spectral analysis. Both methods yielded the most significant peak corresponding to a period of 29 5 days (see Table III) This is the value to be expected for this epoch (1967-68) of the solar cycle when the magnetic activity is at higher latitudes (the synodic equatorial rotation is ≈ 27 days). Thus by this test the technique gives the same result even when applied to data summed over 6 2/3 days (~100 orbits).

As an additional check on the analysis, we subjected various sets of random numbers to the algorithm used and found in those samples no evidence of periodicity at or near the power level found for the Dallas neutron monitor data.

Let us turn now to the results obtained on the analysis of the actual data. The data of Figs. 18-21 have been subject to the Fourier Analysis referred to. Where a data point had no data, the average value was inserted and for the data of Figs. 18 and 19 the analysis was done in two ways one used the data as given (a) and the other replaced the peaks around orbits 33-35 with the average value; the results (i e. the comparison of Tables 1-a and 1-b) are not overly sensitive to this, particularly the period with the most power. The data are presented in Tabular form in Table III where the periods having the most power are given in decreasing order of power. There appears to be evidence for a period of about 25 days (the equatorial solar rotation period with respect to the galaxy), rather than a synodic period. This is in itself puzzling. On the other hand, it may be possible that due to the complicated superposition of satellite orbit with earth rotation, and the orbital motion of the earth, that many possible periods could emerge. Though no such analysis has been carried out, the unphysical aspect of a non-synodic solar rotation period would tend toward the latter type explanation.

In any event, it does appear reasonably justified to lump our data the way we have and to do our analysis on the data summed over the entire orbital period. With respect to the anomalous fluctuations seen in the AC and AC$\overline{D}$ channels, but not the proton (AB$_p$C$\overline{D}$) channel we have no explanation. We have searched the Solar-Geophysical reports for the appropriate time periods and have been unable to find any phenomena to correlate. It is worth emphasizing that since the fluctuations did not appear in the proton channel, which is directly sensitive to the primary cosmic radiation, but in the AC and AC$\overline{D}$ channels which are sensitive to ambient particles, that it could represent a local rather than a Solar-Geophysical event. We cannot rule out temporary instrument malfunction, but we find no basis for introducing this as an explanation, particularly since the albedo channels showed this differently

B-Charged Particle Results

The principal results on charged particles are presented in publication-5 and here we will just expand somewhat on these.

We first present data on the calibration made. Fig. 22 presents a comparison of the Mode II response for pre-launch, and post-launch divided into Primary (0-90°) and Albedo (90°-180°) particles. The 10% gain shift is evident in this comparison. Fig. 23 shows a comparison of Mode II data for the selection 0°-30° and 150°-180° The enhanced number of particles in the P_1-bin clearly reflects the lowered velocity distribution of upward moving particles. The Mode II response was stable for the entire period of data collection

Figs. 24 and 25 show the angular dependence of the various counting rates for two different rigidity intervals (Vertical Cut-Off) of 4.3-52 Bv and 12.5-15 Bv. This is the basis referred to in the text for the conclusion that the $AB_p C\bar{D}$ and $A'B_1C'$ channels are contaminated. These figures are also the basis for using the angular interval 0-60° for data analysis since it is for $\theta > 60^{\circ}$ that the counting rates fall off.

Fig. 26 shows the Cerenkov response as a function of rigidity for protons (A=Z) and nuclei (A=2Z). This is the basis for the correction required resulting from the use of fixed discriminator levels. The rest of the paper is self-contained.

<u>C-γ-ray Results</u>

We refer here to paper 6 of the publication list. This paper is quite self-contained. We would note several points.

Our albedo measurements are in agreement with those of Fichtel (Table I of publication 6). Our counting rates are in agreement with those of Clark et al. in Explorer XI but not those of Clark et al. in OSO-III (Table II of publication 6) Our flux values are in reasonable agreement with both Explorer XI and the MIT OSO-III results (Table III of publication 6). However, we find no evidence of a line source at the level originally reported by Clark et al. from OSO-III (1968) but cannot contradict or confirm the revised value (Garmire 1970) at a lower intensity.

We append copies of the print out of the cut-off values calculated as a function of zenith and azimuth referred to in the text of publication 5.

Summary of Significant Milestones

Proposal Submitted to NASA	27 July, 1962
Proposal Approved	9 November, 1962
Work Statement for Sub-Contractor Bids Distributed	November, 1962
Evaluation of Sub-Contractor Bids and Selection of BBRC (Ball Bros. Research Corporation)	31 January, 1963
Funding of Contract to University of Rochester	15 February, 1963
Sub-Contract Award to BBRC	25 February, 1963
Engineering Model Delivered by BBRC to U of R for Test and Evaluation	21 May, 1963
Engineering Model Flown on High Altitude Balloon	19 July, 1963
Modified Engineering Model Reflown on High Altitude Balloon - Not Recovered	8 December, 1963
Prototype Qualification Completed	23 October, 1963
Formal Acceptance of Prototype Performance	19 December, 1963
Major Component Change in Prototype (P.M. tube) Found Necessary	7 April, 1964
Prototype After Modification Requalified and Accepted	15 April, 1964
Flight Model Delivered for S-57 Experiment Integration to BBRC	19 May, 1964
Flight Spare Delivered for Experiment Integration to BBRC	3 December, 1964

OSO-C Launch-Orbit Not Attained	August, 1965
Flight Spare Refurbished and Delivered for Experiment Integration to BBRC	15 May, 1966
Successful Launch and Orbit	8 March, 1967

TABLE I

Data Channel	Cts./Min.	Orientation
$ACB_p^1\bar{D}$ (P_1)	$.0294 \pm .0014$	Vertical
$ACB_p^2\bar{D}$ (P_2)	$.173 \pm .0035$	"
$ACB_p^3\bar{D}$ (P_3)	$.443 \pm .0056$	"
$ACB_p^4\bar{D}$ (P_4)	$.169 \pm .0035$	"
$ACB_p^5(\bar{D})$ (P_5)	$.0256 \pm .002$	"
$ACB_p^6\ (\bar{D})$ (P_6)	$.012 \pm .0009$	"
$ACB_p\bar{D}$	$.84 \pm .0068$	"
AC	$1.005 \pm .036$	"
$AC\bar{D}$	$.813 \pm .025$	"
$ACB\ \bar{D}$ (He)	$.00076 \pm .004$	"
$\bar{X}AB_\gamma C\bar{D}$ (γ)	$.001 \pm .0005$	"
$A'B_LC'$ (L)	0	"
$A'B_MC'$ (M)	0	"
$A'B_HC'$ (H)	0	"
AC	$.0706 \pm .006$	Horizontal
$AC\bar{D}$	$.0074 \pm .002$	"
$AB_pC\bar{D}$	$.0103 \pm .002$	"
$\bar{X}AB_\gamma C\bar{D}=ACB\ \bar{D}=A'B_LC'=$ $A'B_MC'=A'B_HC'=0$	0	Inverted & Horizontal
$AB_pC\bar{D} = AB_p^1C\bar{D}$	$.0096 \pm .0018$	Inverted

TABLE II-1

S-57 Prototype Detector

1 Flight on 3 October 1964

Launch:	0600
Begin Float:	0830
Cut Down:	1742
On Ground:	1815

1. Pre- and Post-Flight Mode II distributions in agreement
2. 9 15 hours of data obtained at altitude of 4 to 4.5 gm/cm^2
3. γ-ray channel did not operate during flight
4. B channel threshold levels: (before flight) in 2 x 1/8 channels

	Lower	Upper
B_p^1	20	55.5
B_p^2	55.5	86
B_p^3	86	116
B_p^4	116	147
B_p^5	147	177
B_p	20	262.5
B	262.5	686
B_L	747	3230
B_M	3230	9400
B_H	9400	--

Peak of Sea-level μ dist.:

Before Flight: 95 ch's

After Flight: 94 ch's

FWHM: 64%

TABLE II-2

S-57

Logic	Counts	Time	Rate
A_1C_1	17,539	548.87	31.95 ± 0.25
$A_1C_1\overline{D}$	5,475	453.76	12.07 ± 0.16
$A_1C_1B_p\overline{D}$	3,617	453.76	7.97 ± 0.13
$A_1C_1B\ \overline{D}$	359	416.91	0.861 ± 0.046
$A_2C_2B_L\overline{D}$	4	416.91	0.0096 ± 0.0048
$A_2C_2B_M\overline{D}$	6	416.91	0.0144 ± 0.007
$A_2C_2B_H\overline{D}$	1	416.91	0.0024 ± 0.0024
A_2C_2	292	462.92	0.631 ± 0.037
$A_2C_2\overline{D}$	31	416.91	0.074 ± 0.013
$A_2C_2B_p\overline{D}$	0	416.91	0.0
$A_2C_2B\ \overline{D}$	1	416.91	0.0024 ± 0.0024
$A_1C_1B_p$	1403	95.11	14.75 ± 0.40
A_1C_1B	108	46.01	2.35 ± 0.20
$A_2C_2B_p$	7	46.01	0.15 ± 0.054
A_2C_2B	3	46.01	0.065 ± 0.037
$A_2C_2B_L$	33	462.92	0.0713 ± 0.012

TABLE II-2

S-57

Logic	Counts	Time	Rate
$A_2C_2B_M$	48	462.92	0.104 ± 0.015
$A_2C_2B_H$	16	462.92	0.0346 ± 0.00865
$\overline{X}A_1C_1B_\gamma\overline{D}$	--	--	--
$\overline{X}A_1C_1B_\gamma$	--	--	--

	Times
Mode I, $\overline{D}$ Active	416.91 mins.
Mode I, $\overline{D}$ Disabled	46.01
Mode II, $\overline{D}$ Active	36.85
Mode II, $\overline{D}$ Disabled	49.10
Total	548.87 mins. or 9.15 hours

TABLE II-2

S-57

Logic	Counts	Time	Rate
$A_1C_1B_p^1\bar{D}$	17	36.85	0.461 ± 0.10
$A_1C_1B_p^2\bar{D}$	56	36.85	1.53 ± 0.20
$A_1C_1B_p^3\bar{D}$	87	36.85	2.360 ± 0.24
$A_1C_1B_p^4\bar{D}$	78	36.85	2.118 ± 0.24
$A_1C_1B_p^5\bar{D}$	30	36.85	0.814 ± 0.15
$A_1C_1B_p^6\bar{D}$	4*	36.85	0.1* ± 0.05
$A_1C_1B_p^1$	132	49.10	2.69 ± 0.18
$A_1C_1B_p^2$	162*	49.10	3.3 ± 0.26
$A_1C_1B_p^3$	191	49.10	3.89 ± 0.28
$A_1C_1B_p^4$	157	49.10	3.20 ± 0.25
$A_1C_1B_p^5$	72	49.10	1.467 ± 0.18
$A_1C_1B_p^6$	28*	49.10	0.57* ± 0.11

*these values inferred

TABLE III

Fourier Analysis of Dallas Neutron Monitor Data for Period Covering Orbits 1-5600 of OSO-III

Daily Data		Lumped (100 orbits) Data	
Period (Days)	Power (Arb. Units)	Period (Days)	Power (Arb. Units)
29.5 ± 0.7	.843	30.0 ± .8	.858
16.5 ± 0.3	.283	16.9 ± .4	.265
22.0 ± 0.5	.214	22.2 ± .6	.180

TABLE IV

Fourier Analysis For Data of Figures 17-21
The period for a given coincidence channel is given in days and the power in that frequency is given (in arbitrary units) in ( ) following the period. The three dominant periods are listed.

1-a

$0 \leq ZA \leq 60^{\circ}$	$3.0 \leq R_V(Bv) \leq 4.3$	Peaks in orbits 33-35 included
AC	$AC\overline{D}$	P
24.6 ± 0 7 (7.32)	24.6 ± 0.35 (13.0)	50.6 ± 1.4 (7.08)
93.2 ± 1.4 (6.88)	49.2 ± 1.4 (10.4)	27 ± 0.7 (6.91)
49.8 ± 1.4 (6.55)	93.2 ± 0.7 (9.91)	110 ± 10 (3.13)

1-b

$0 \leq ZA \leq 60^{\circ}$	$3 \leq R_V(Bv) \leq 4.3$	Peaks at 33-35 replaced by average values
AC	$AC\overline{D}$	P
25.3 ± 0.7 (7.6)	24.7 ± 0.7 (13.9)	50.6 ± 1.4 (7.1)
52.5 ± 2.0 (2.4)	50.5 ± 0.7 (6.2)	27 ± 0.7 (6.91)
16 2 ± 0.7 (1.2)	93.2 ± 1 4 (2.32)	34 ± 1.4 (2.89)

TABLE IV (Cont'd)

2-a

$0 \leq ZA \leq 60^{o}$	$12.5 \leq R_V(Bv) \leq 15$	Peaks in orbits 33-35 replaced by average values
AC	AC$\overline{D}$	P
25 $\pm$ 0.7 (31.6)	25 $\pm$ 0.7 (10.3)	25.3 $\pm$ 0.7 (5 5)
41.4 $\pm$ 1.4 (2.2)	41.4 $\pm$ 1.4 (1.9)	51.4 $\pm$ 0.7 (2.2)
53.4 $\pm$ 1.4 (1.8)	53.4 $\pm$ 1.4 (1.7)	16.9 $\pm$ 0.5 (1.7)

3

$120 \leq ZA \leq 180^{o}$	$3 \leq R_V(Bv) \leq 4.3$	
AC	AC$\overline{D}$	P
53.2 $\pm$ 1.4 (2.8)	69.2 $\pm$ 1.4 (17.3)	48.5 $\pm$ 1.4 (25.4)
29.9 $\pm$ 2.8 (86)	28.3 $\pm$ 1.4 (3.81)	24.6 $\pm$ 0.7 (21.2)
21.9 $\pm$ 1.4 (.83)	41.2 $\pm$ 1.4 (2.70)	93.0 $\pm$ 1 4 (7.3)

4

$120 \leq ZA \leq 180^{o}$	$12.5 \leq R_V(Bv) \leq 15$	
AC	AC$\overline{D}$	P
25.3 $\pm$ 0.7 (22.7)	25.0 $\pm$ 0.7 (5.46)	25.0 $\pm$ 0.7 (5.5)
41.2 $\pm$ 1.4 (2.13)	42.5 $\pm$ 1.4 (1.84)	51.2 $\pm$ 1.4 (2.2)
33.3 $\pm$ 1.4 (1.76)	186.5 $\pm$ 18 (1 78)	16.7 $\pm$ 1.4 (1.6)

Publications

(1) "Sensitivity of Cosmic Gamma-Ray Telescopes", B R. Dennis and G. Share, Nucl. Instr. and Methd's., 50, (1967), 100-104.

(2) "High Energy Proton, Helium and Gamma-Ray Observations on OSO-III, M. F. Kaplon, D. Valentine, Solar Physics, 6, (1969), 216-227.

(3) "High Energy Charged Particle Observations on OSO-III", D. Valentine, M. F. Kaplon, G. Badhwar, Proc. 11th Int. Con. on Cosmic Rays, Budapest 1969, Acta Physica Academiac Scientiarum Hungaricae, 29, Suppl. 1, (1970), 101-109.

(4) "High Energy Gamma-Ray Observations from OSO-III", D. Valentine, M. F. Kaplon, G. Badhwar, 11th Int. Conf. on Cosmic Rays, Budapest 1969, Acta Physica, Academiac Scientiarum Hungaricae, 29, Suppl. 1, (1970), 101-109.

(5) "Charged Particle Observations from OSO-III", G. Badhwar, M. F. Kaplon, D. Valentine, to appear in Journal of Geophysical Research.

(6) "Gamma-Ray Observations from OSO-III", G. Badhwar, M. F. Kaplon, D. Valentine, to appear in Astrophysical Journal.

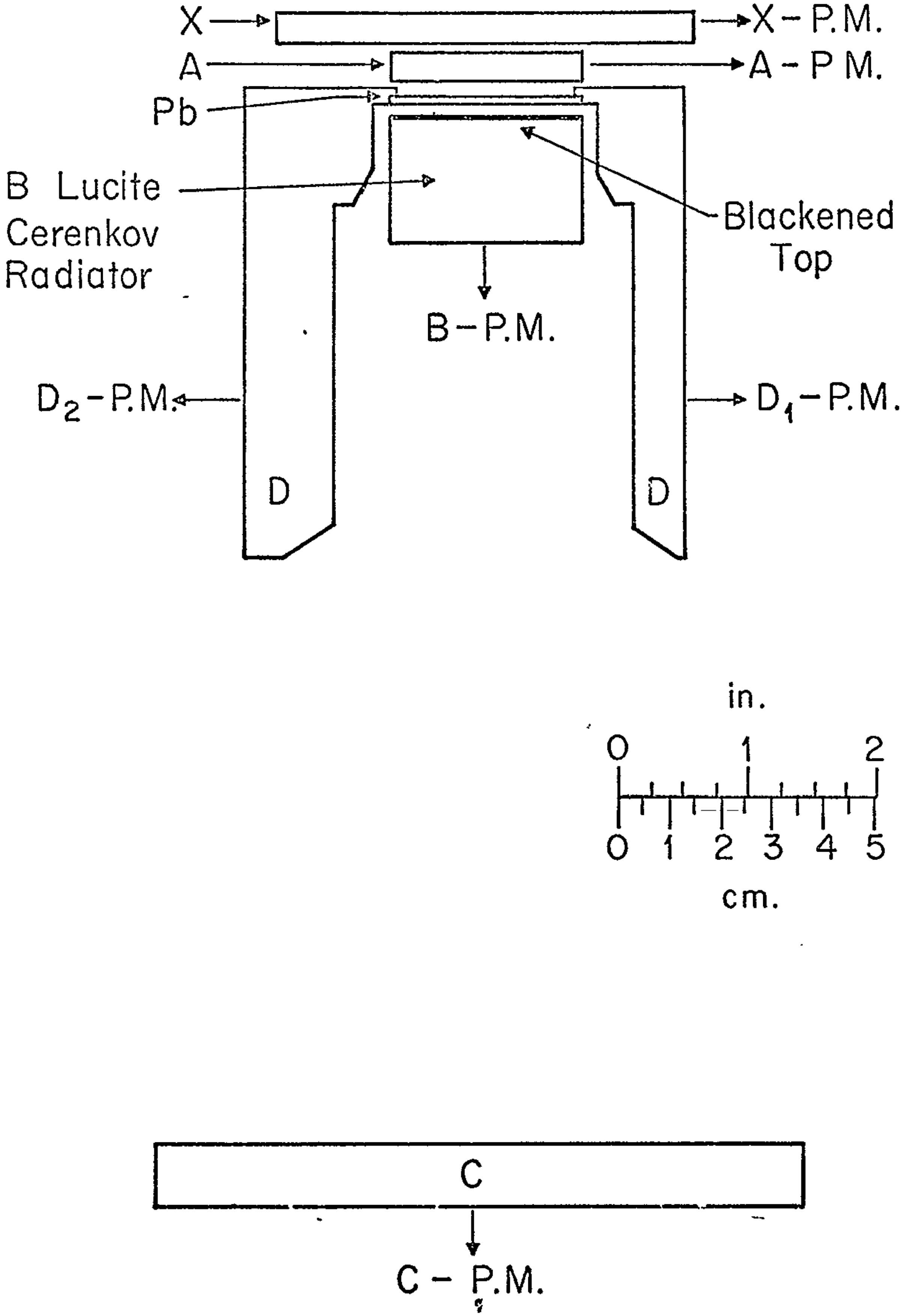
X
X - P.M.
A
A - P M.
Pb
B Lucite Cerenkov Radiator
Blackened Top
B - P.M.
D2 - P.M.
D1 - P.M.
D
D
in.
0 1 2
0 1 2 3 4 5
cm.
C
C - P.M.

FIG. 1

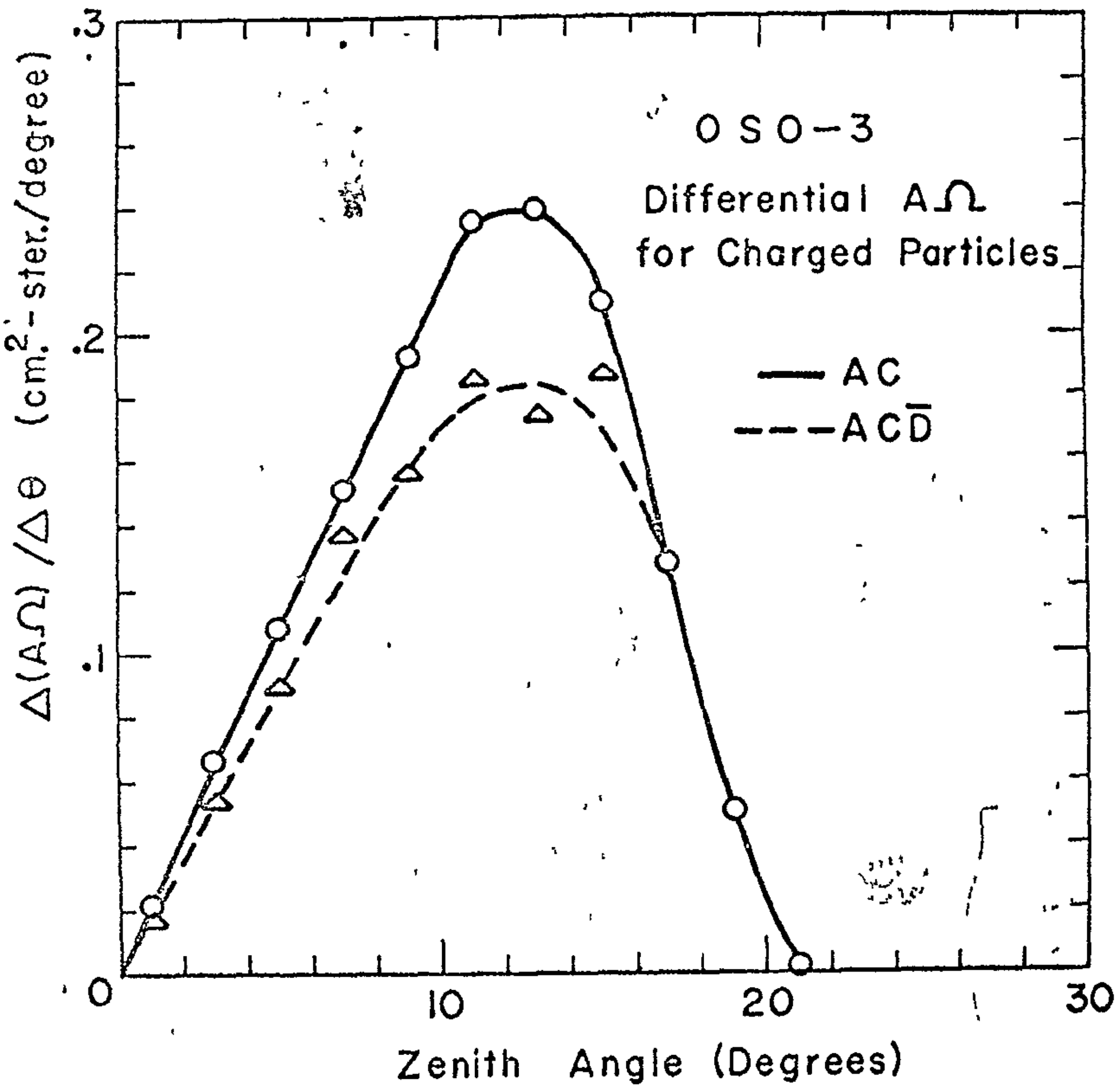
OSO-3
Differential AΩ
for Charged Particles
AC
ACD̄
Δ(AΩ)/ΔΘ (cm.²-ster./degree)
.3
.2
.1
0
10
20
30
Zenith Angle (Degrees)

FIG. 2

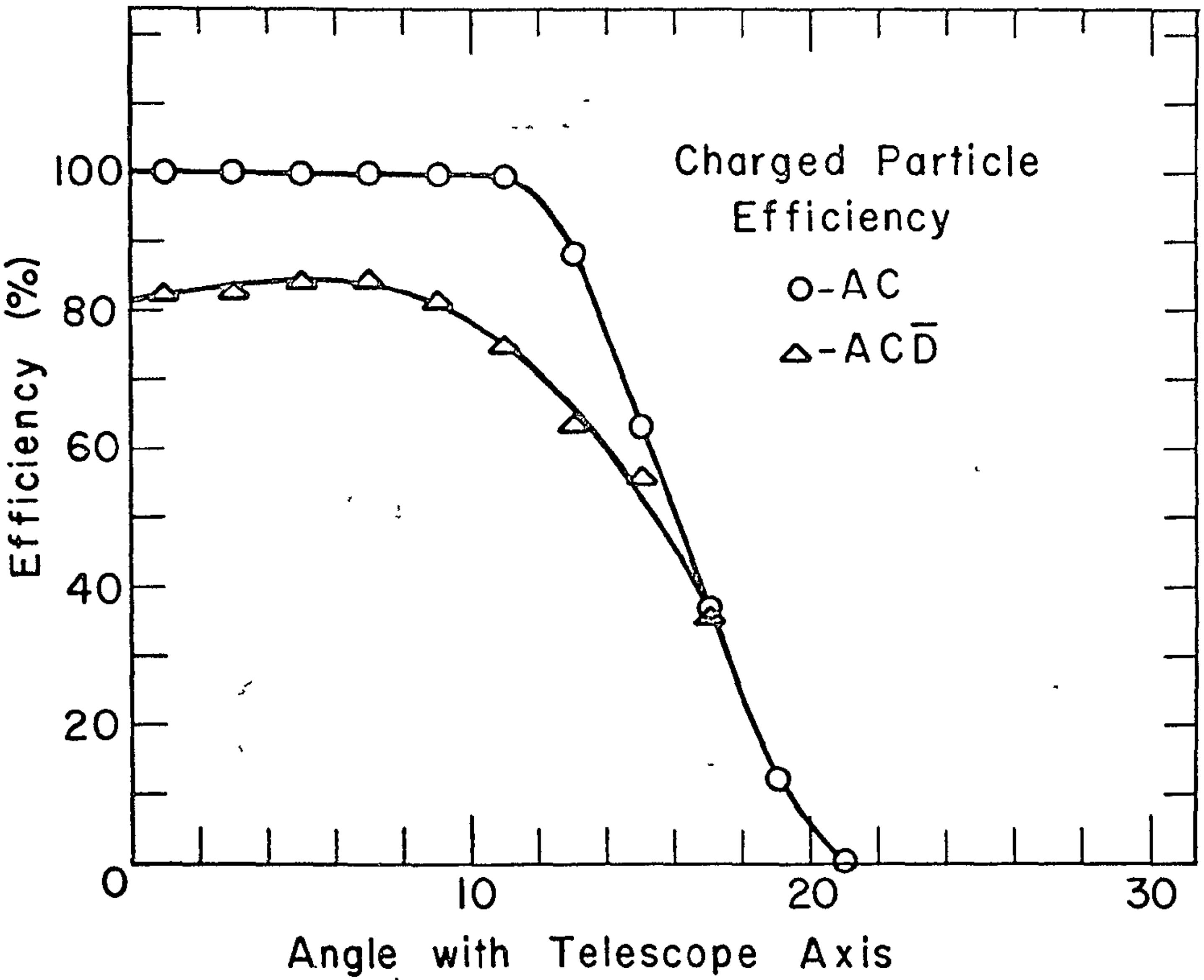

Charged Particle Efficiency
o-AC
△-ACD̄
Efficiency (%)
100
80
60
40
20
0
10
20
30
Angle with Telescope Axis

Fig. 3

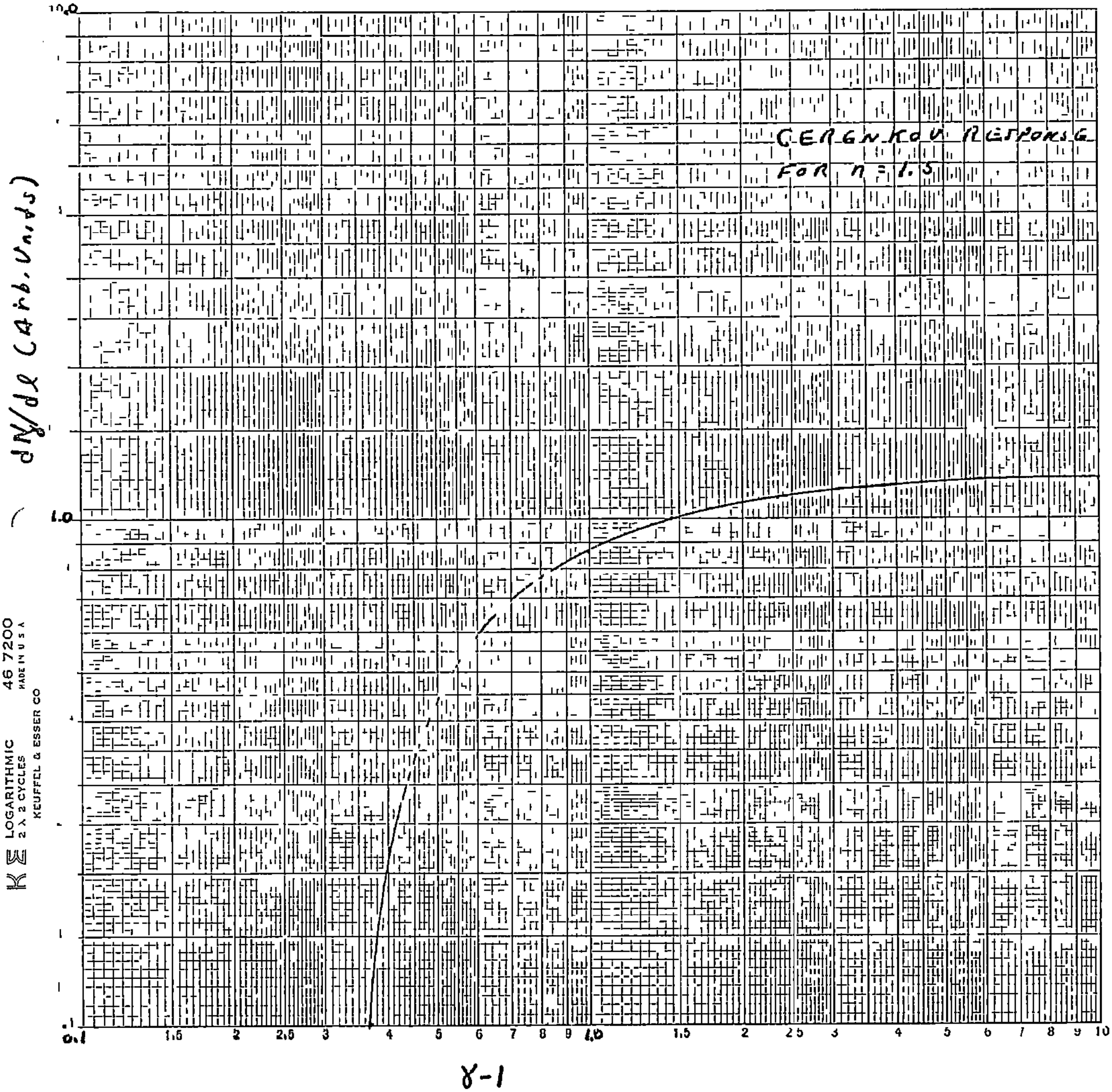
CERENKOV RESPONSE
FOR n = 1.5
dN/dl (Arb. Units)
γ-1
10.0
1.0
.1
0.1
1.5
2
2.5
3
4
5
6
7
8
9
1.0
1.5
2
2.5
3
4
5
6
7
8
9
10
LOGARITHMIC
2 X 2 CYCLES
KEUFFEL & ESSER CO
46 7200
MADE IN U S A

FIG. 4

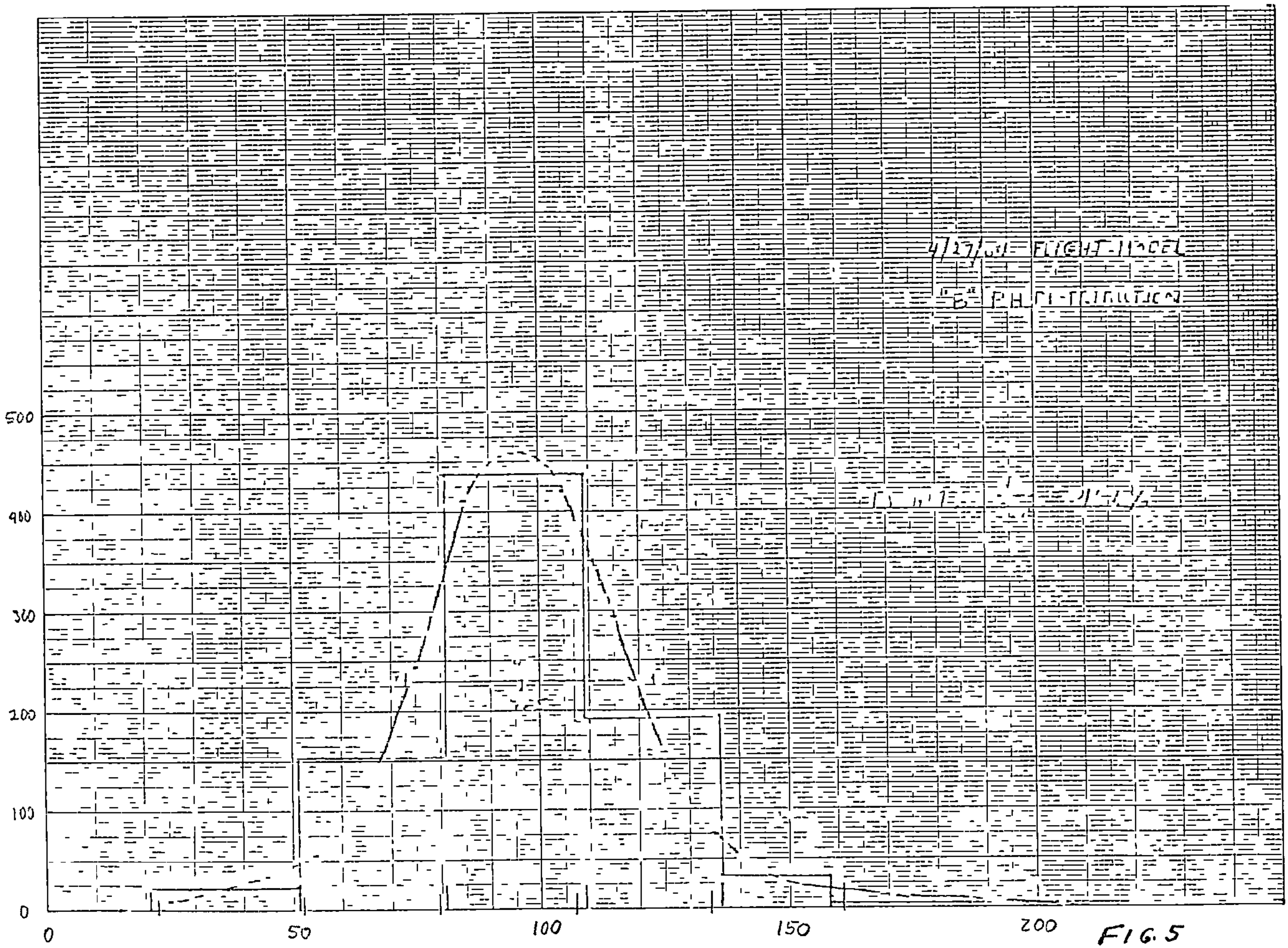

FIG. 5

FOLDOUT FRAME 1

FOLDOUT FRAME 2

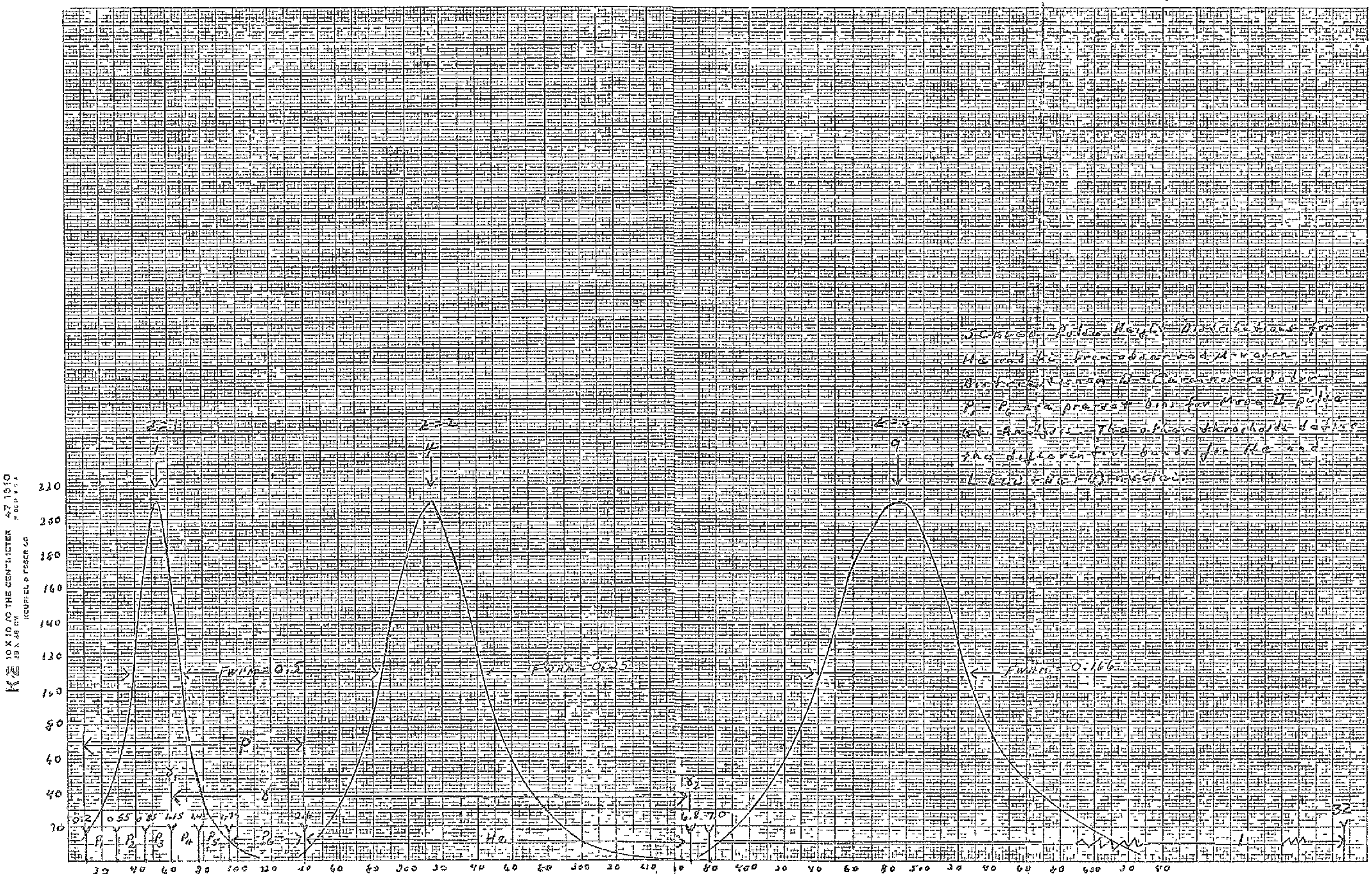

FIG. 6

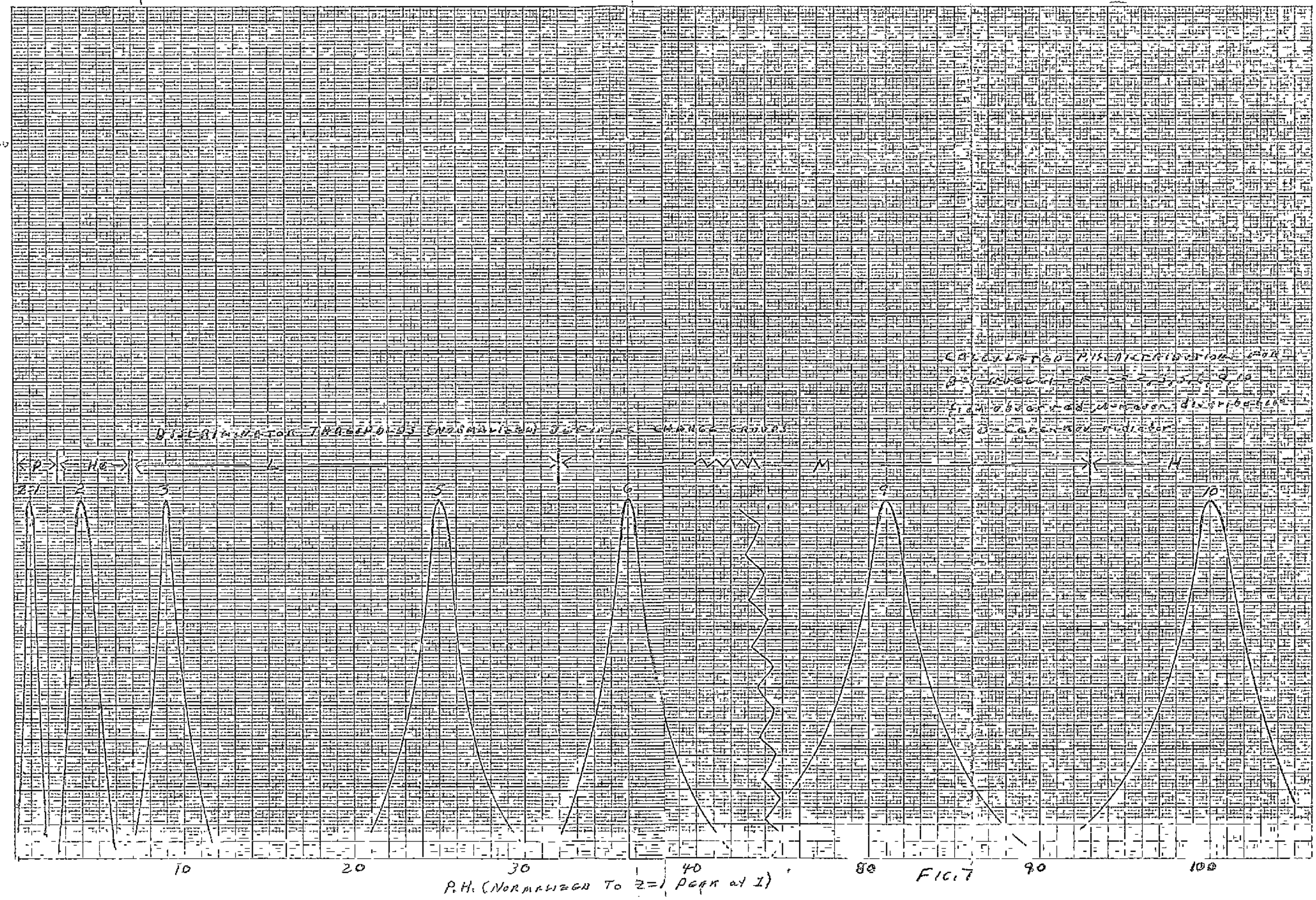
Calculated P.H. distributions for
from observed Landau distribution
Discriminator thresholds (normalized) defining charge groups
P
He
L
M
H
Z=1
2
3
5
6
9
10
10
20
30
40
80
90
100
P.H. (Normalized to Z=1 peak at 1)

FIG. 7

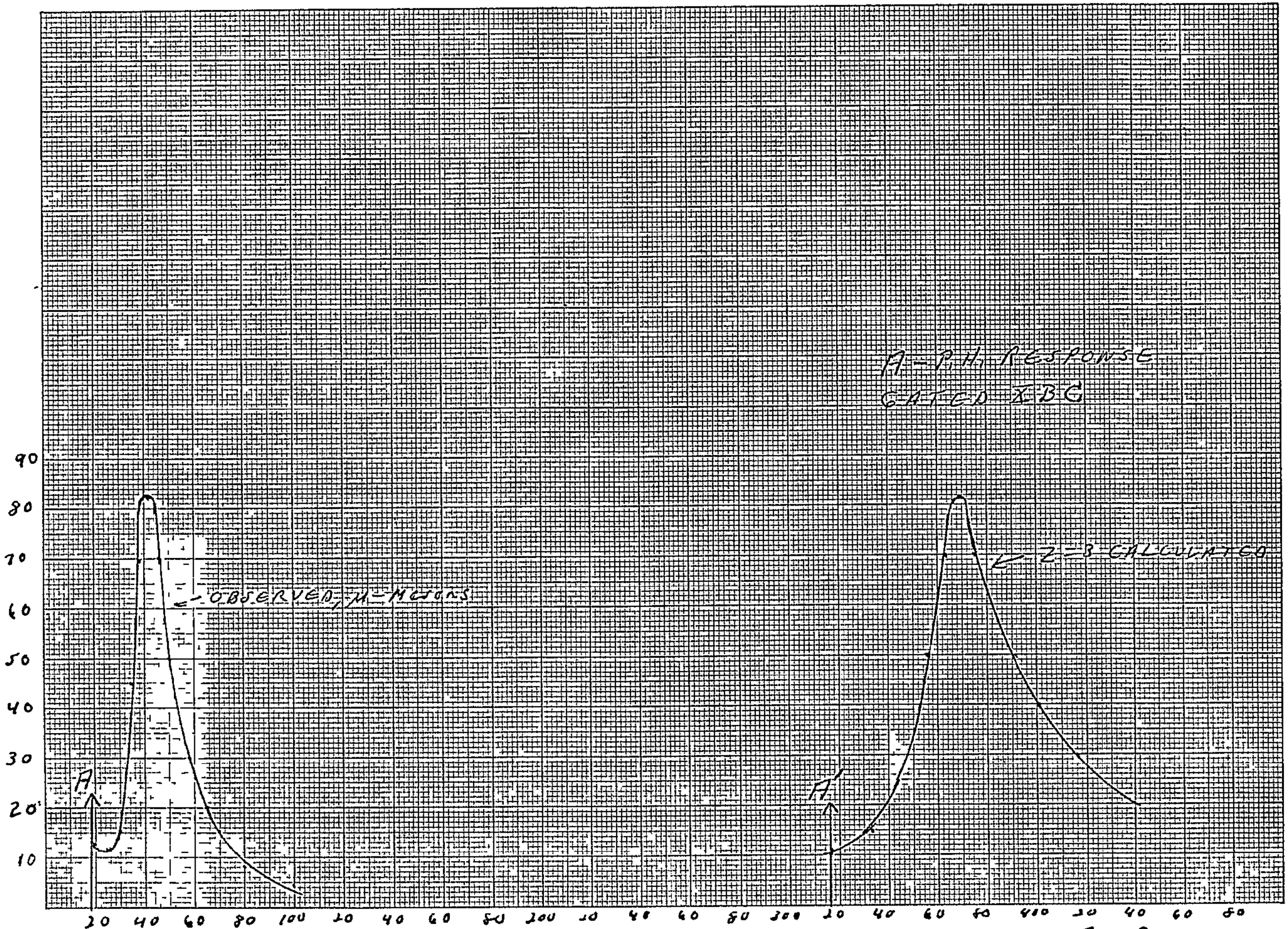
A-P.H. RESPONSE
GATED XBC
90
80
70
60
50
40
30
20
10
A
A'
←OBSERVED, μ-MESONS
← Z-3 CALCULATED
20 40 60 80 100 20 40 60 80 200 20 40 60 80 300 20 40 60 80 400 20 40 60 80
P.H. CH.#

FIG. 8

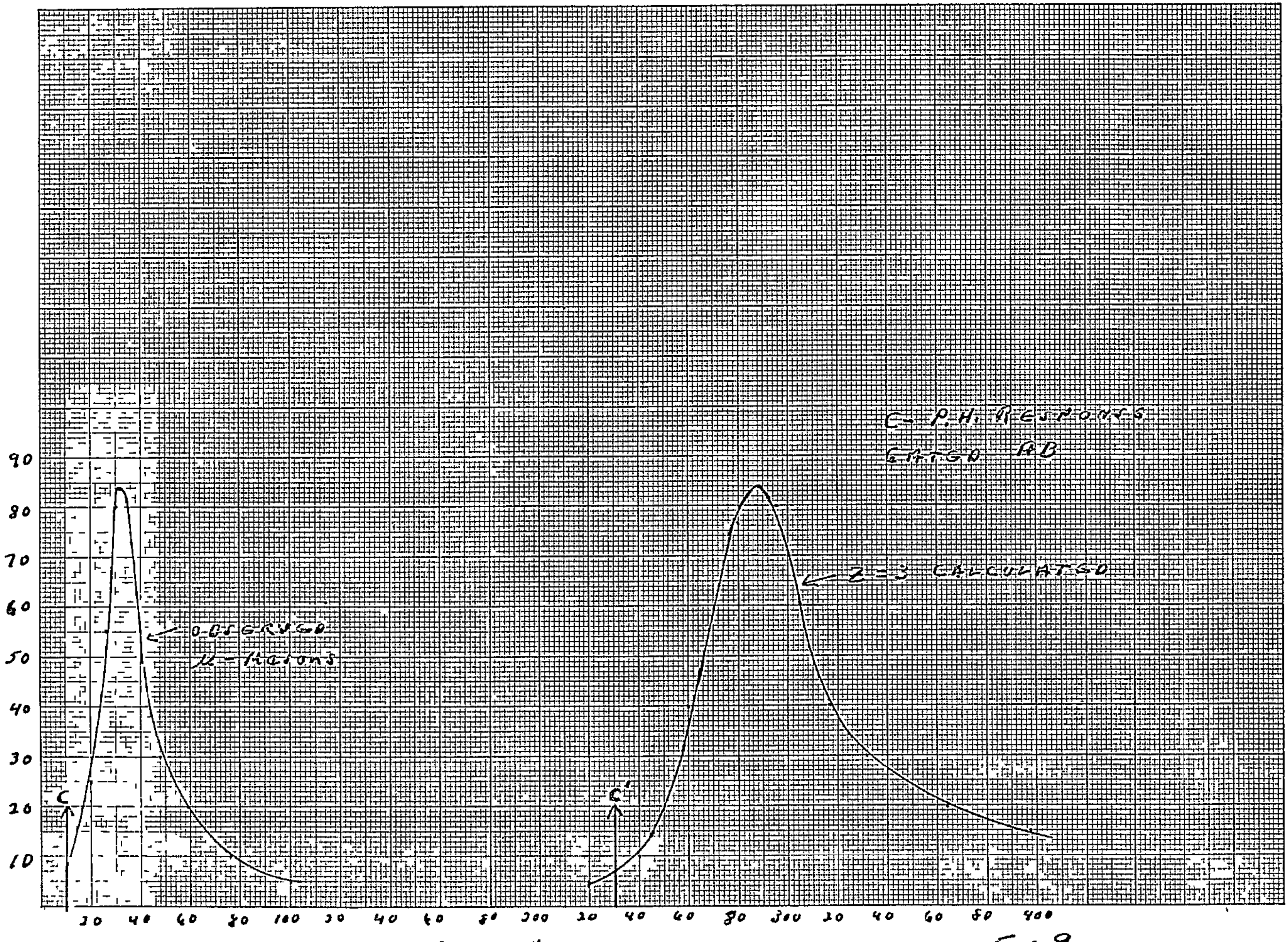
C - P.H. RESPONSE
GATED AB
Z=3 CALCULATED
OBSERVED
μ-MESONS
C
C'
90
80
70
60
50
40
30
20
10
20 40 60 80 100 20 40 60 80 200 20 40 60 80 300 20 40 60 80 400
P.H. CH. #

FIG. 9

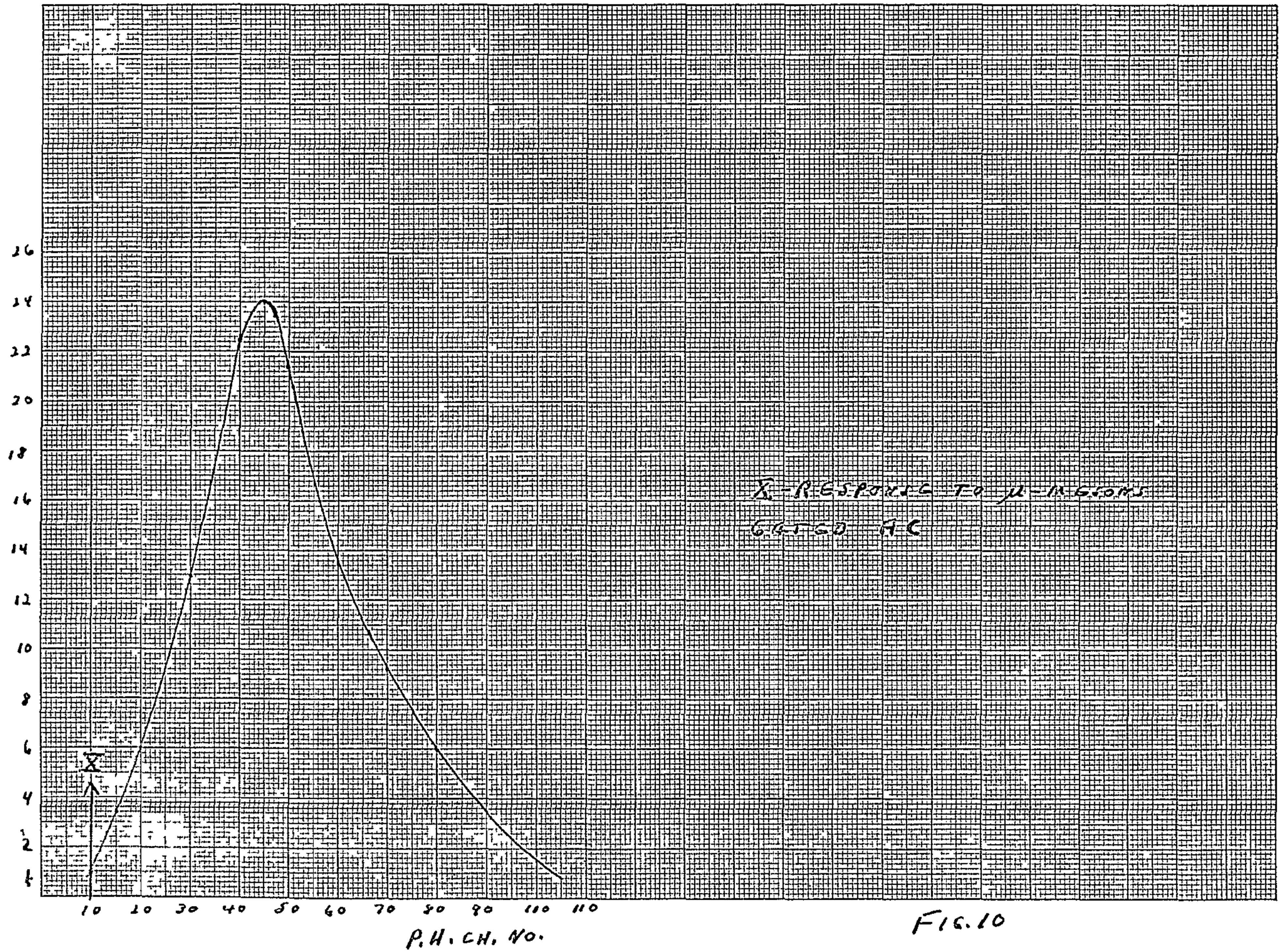
26
24
22
20
18
16
14
12
10
8
6
4
2
X̄
X̄-RESPONSE TO μ-MESONS
10 20 30 40 50 60 70 80 90 110 110
P.H. CH. No.

FIG. 10

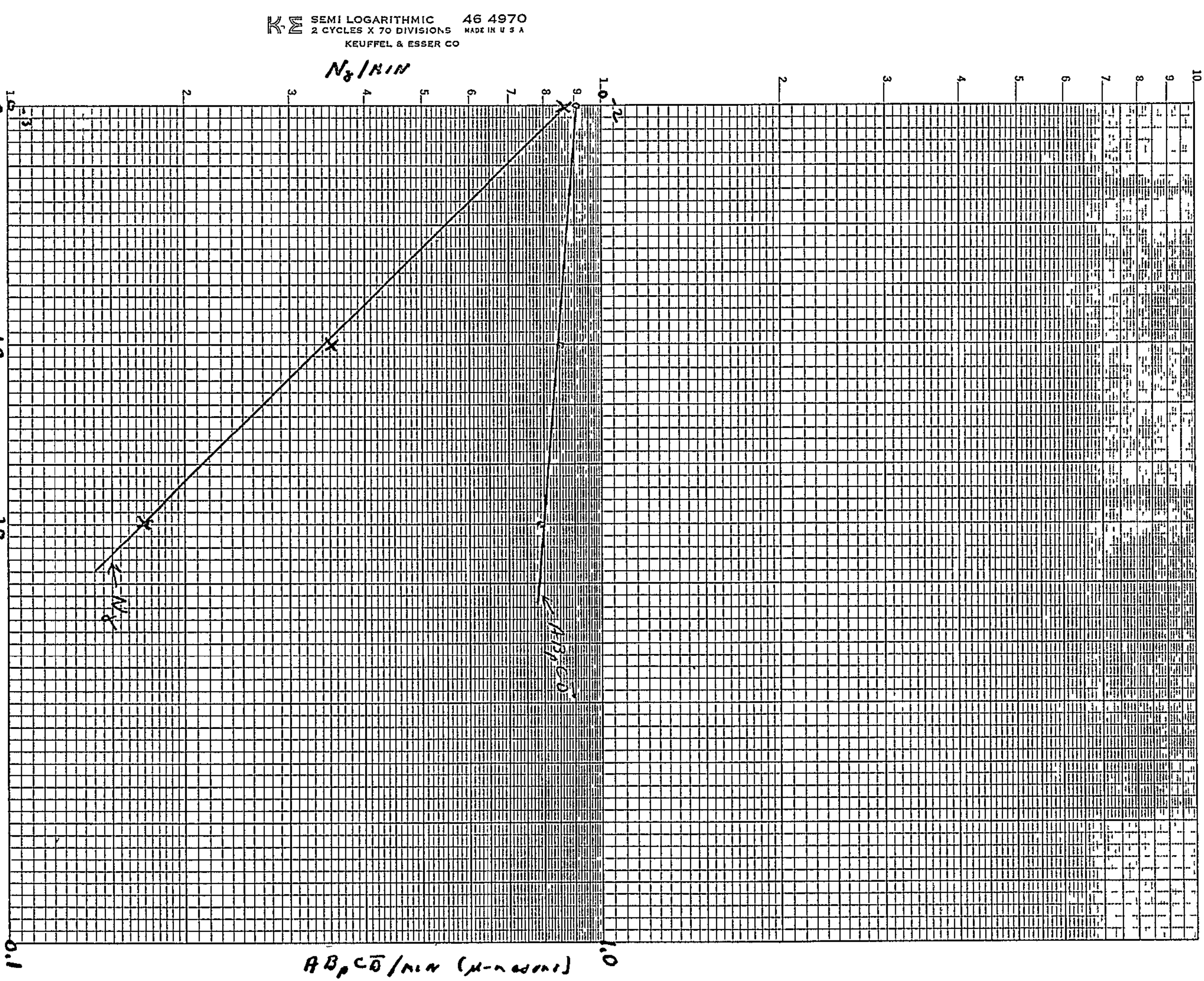
K&E SEMI LOGARITHMIC 46 4970
2 CYCLES X 70 DIVISIONS MADE IN U.S.A.
KEUFFEL & ESSER CO
Nγ/MIN
AB_ρ C D̄/MIN (μ-amps)
Ch. Ab. Overhead
Nγ
AB_ρ C D̄

FIG. 11

DISTRIBUTION IN WORD 47 WORD 1 TOTAL COUNT

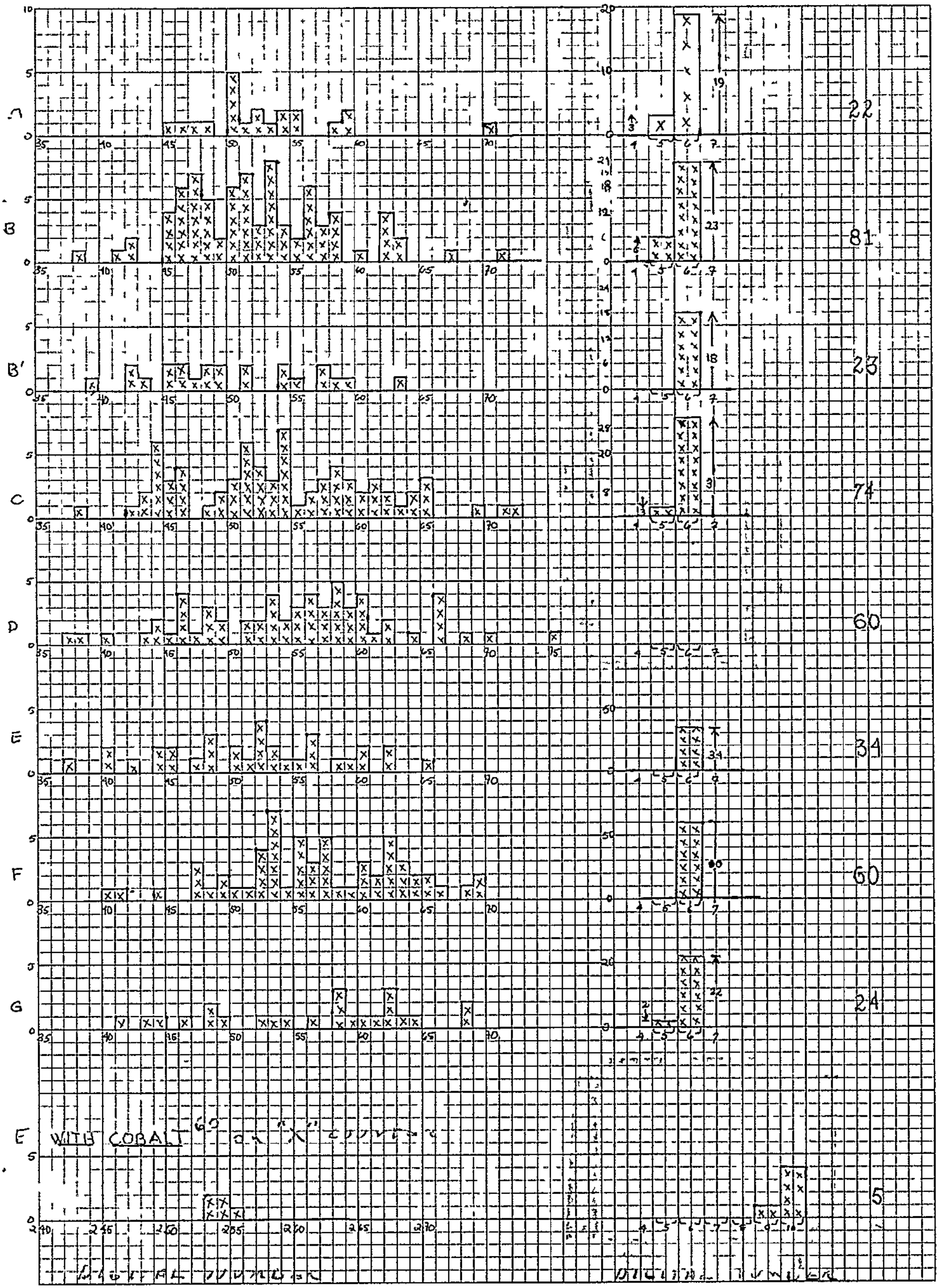

ANALOG CHANNEL FIG. 12

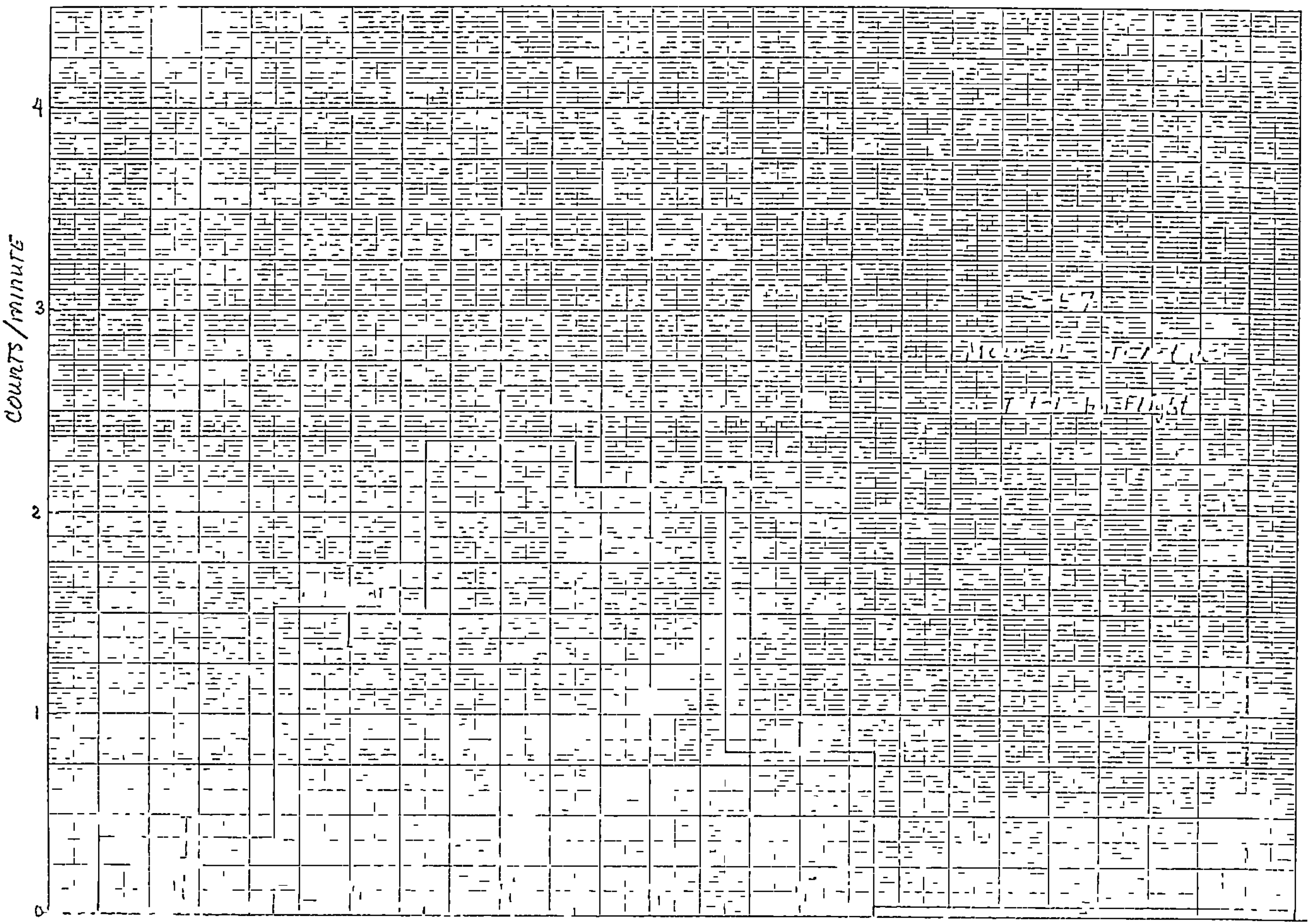

FIG. 13

K+E 10 X 10 TO THE CM 358 14
KEUFFEL & ESSER CO MADE IN U.S.A.

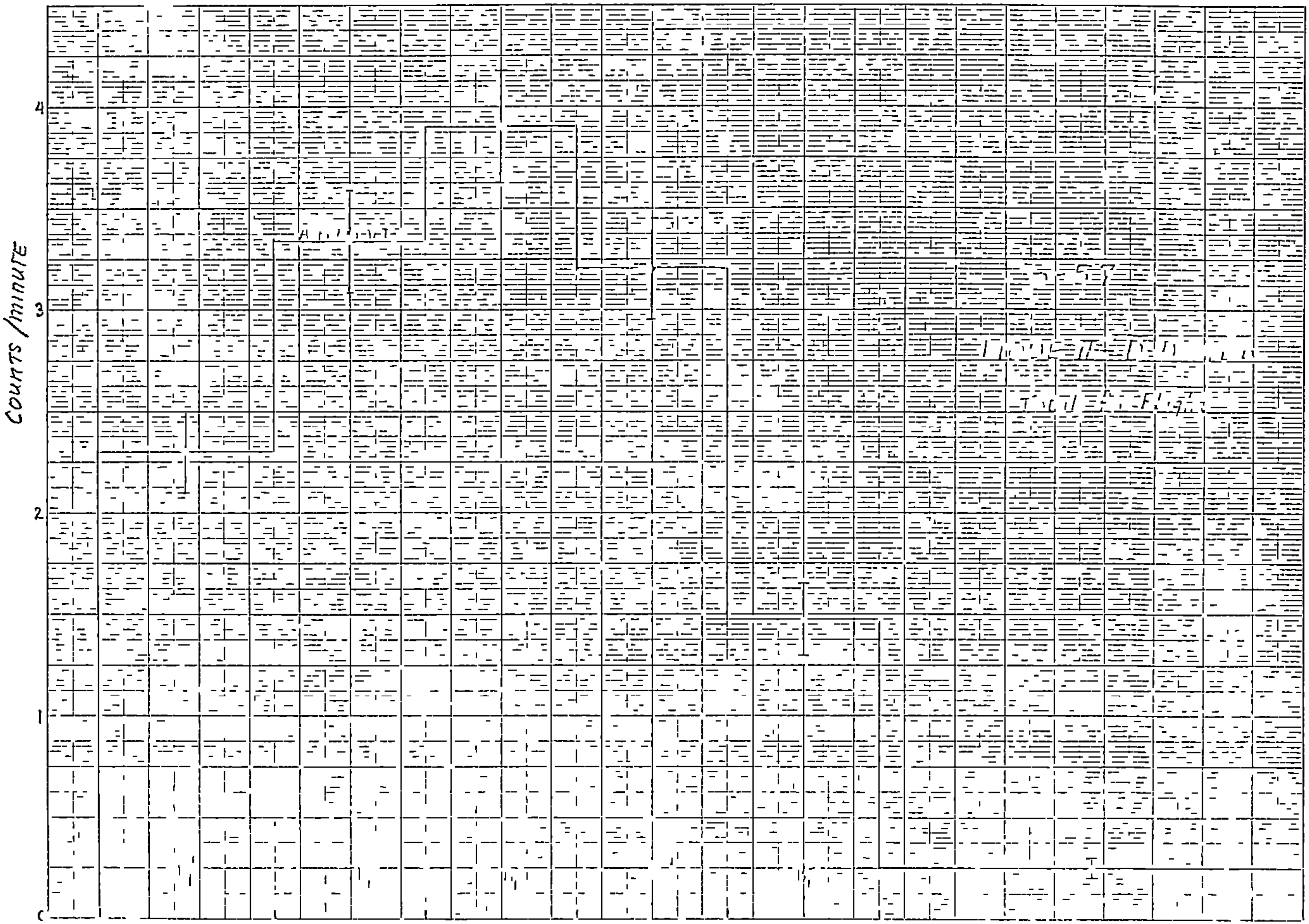

FIG 14

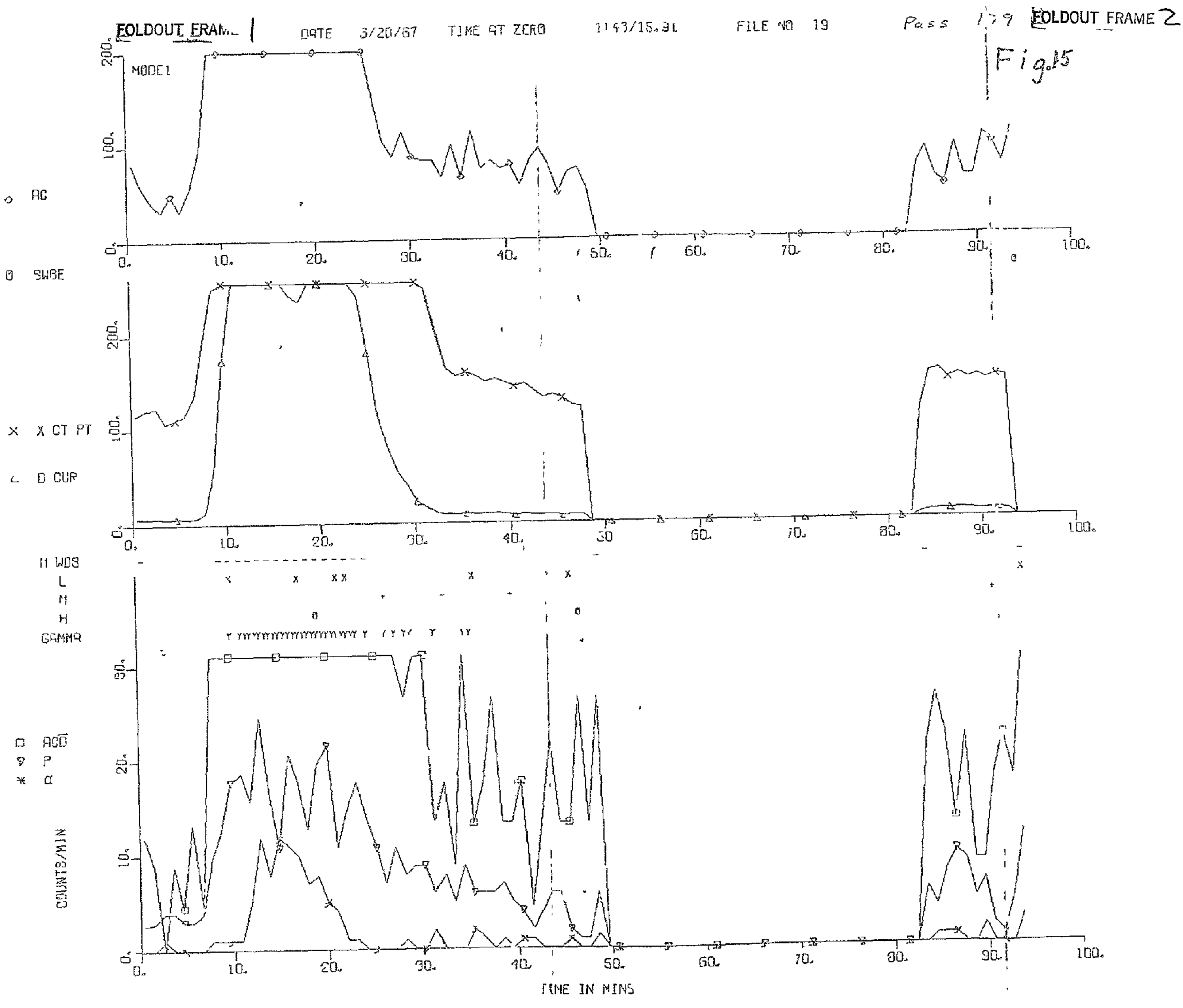
FOLDOUT FRAME 1
DATE 3/20/67
TIME AT ZERO
FILE NO 19
Pass 179
FOLDOUT FRAME 2
Fig. 15
MODE1
AC
SWBE
X CT PT
D CUR
M WDS
L
M
H
GAMMA
ACD
P
α
COUNTS/MIN
TIME IN MINS

FOLDOUT FRAME 1

DATE 3/30/67 TIME AT ZERO 0245/8.90 FILE NO 20 Pass 3 & 4

FOLDOUT FRAME 2

Fig. 16

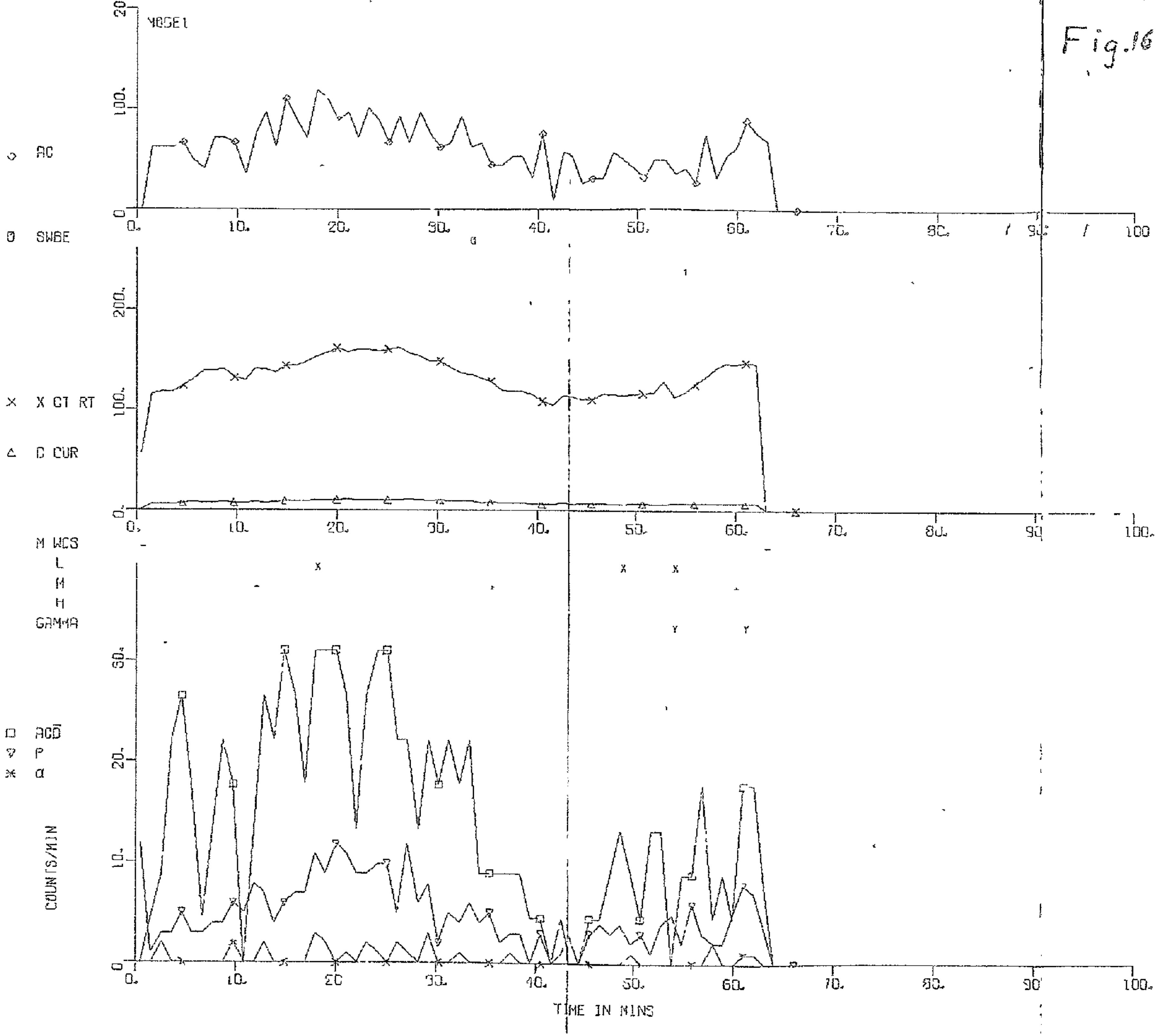

FOLDOUT FRAME 1

FOLDOUT FRAME 2

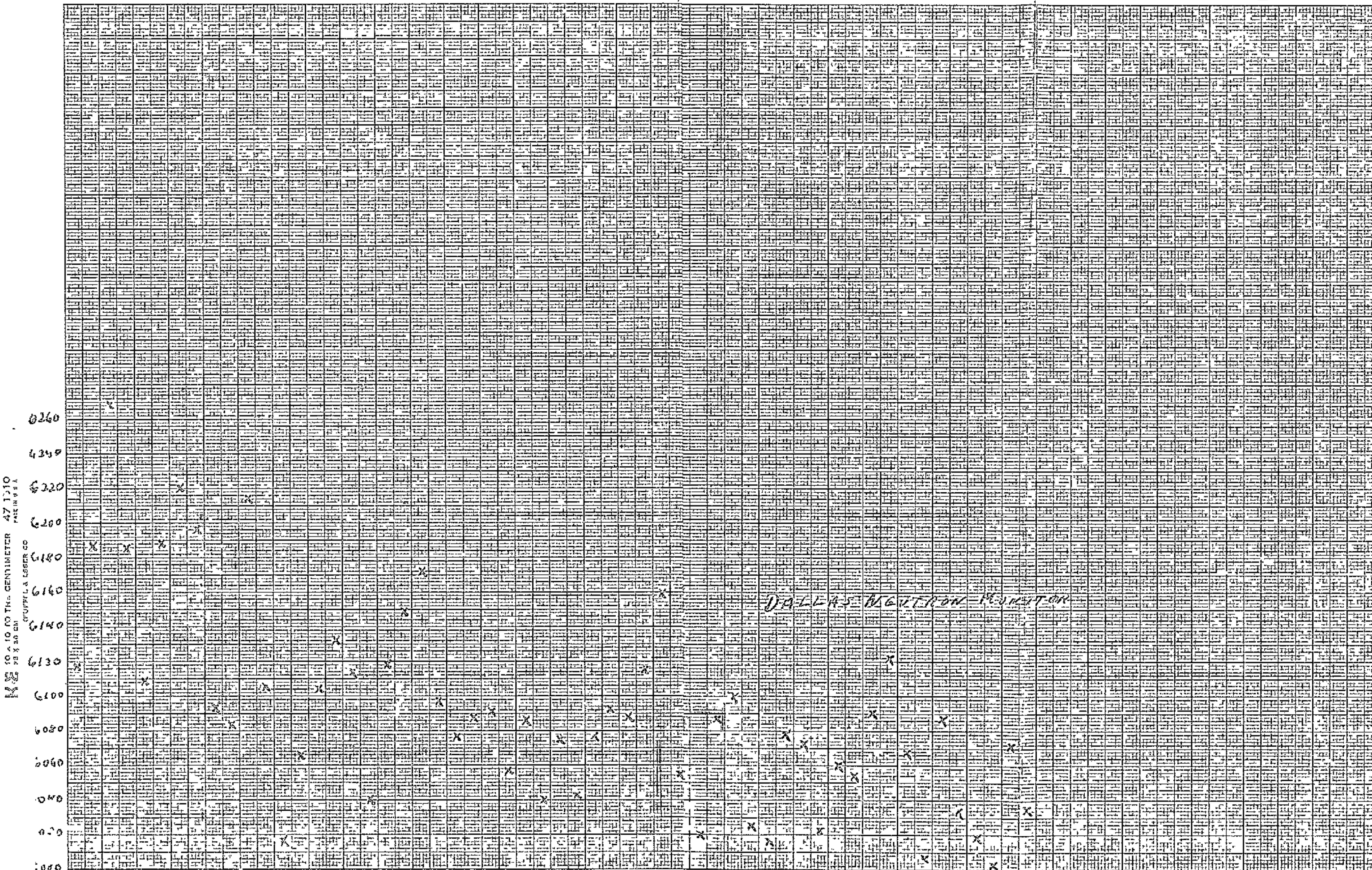

Fig. 17

FOLDOUT FRAME 1

FOLDOUT FRAME 2

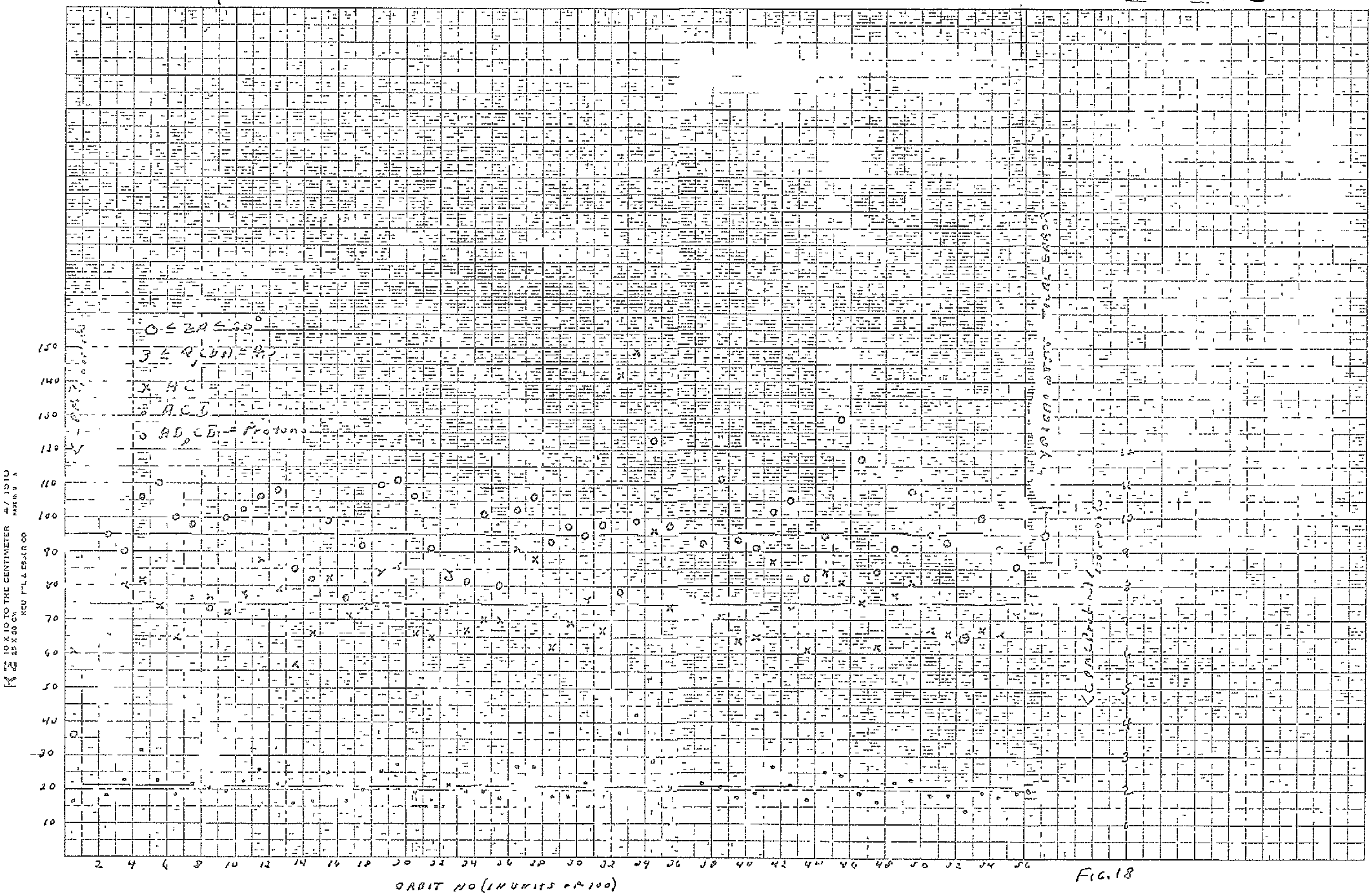

FIG. 18

FOLDOUT FRAME 1

FOLDOUT FRAME 2

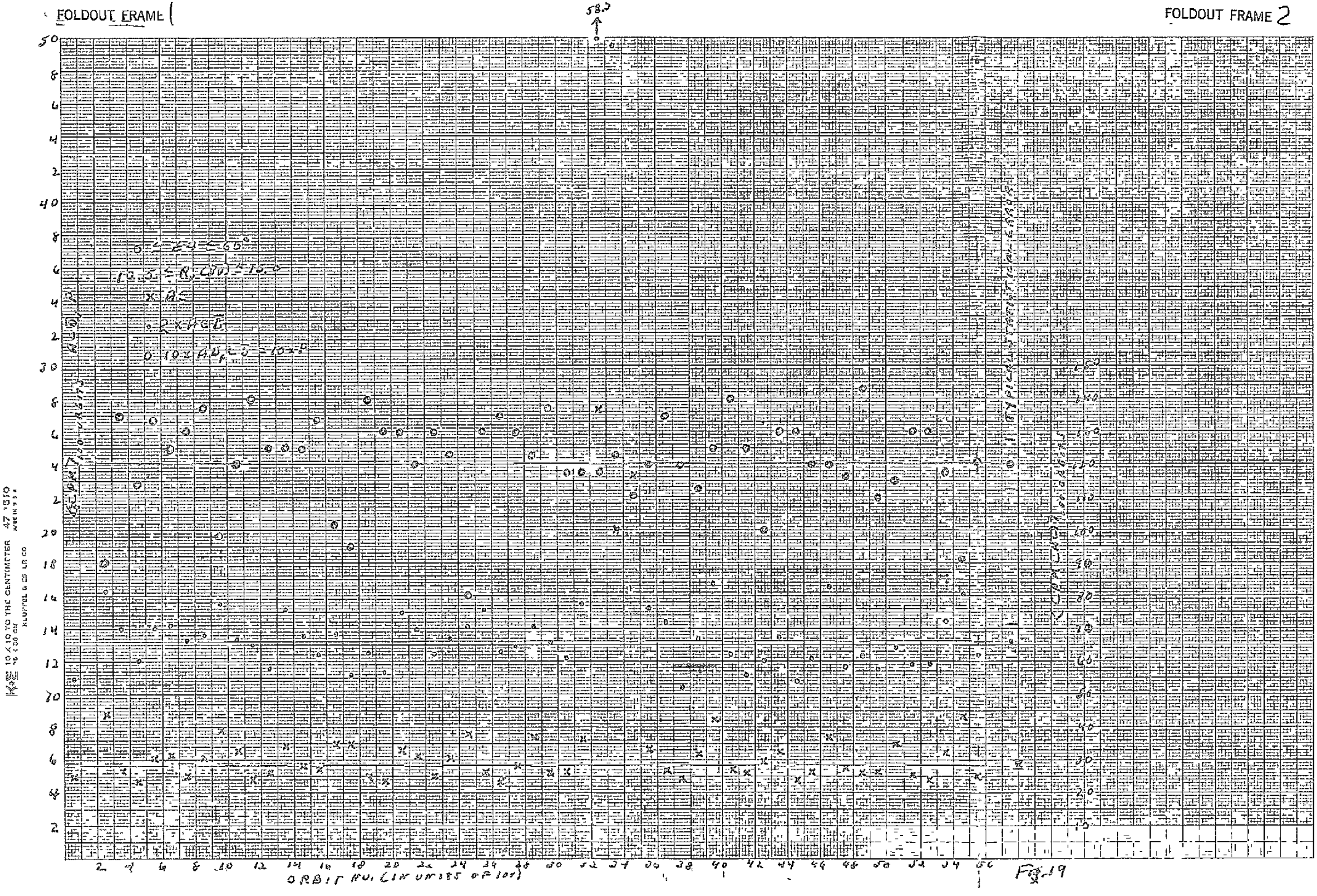

Fig. 19

FOLDOUT FRAME 1

FOLDOUT FRAME 2

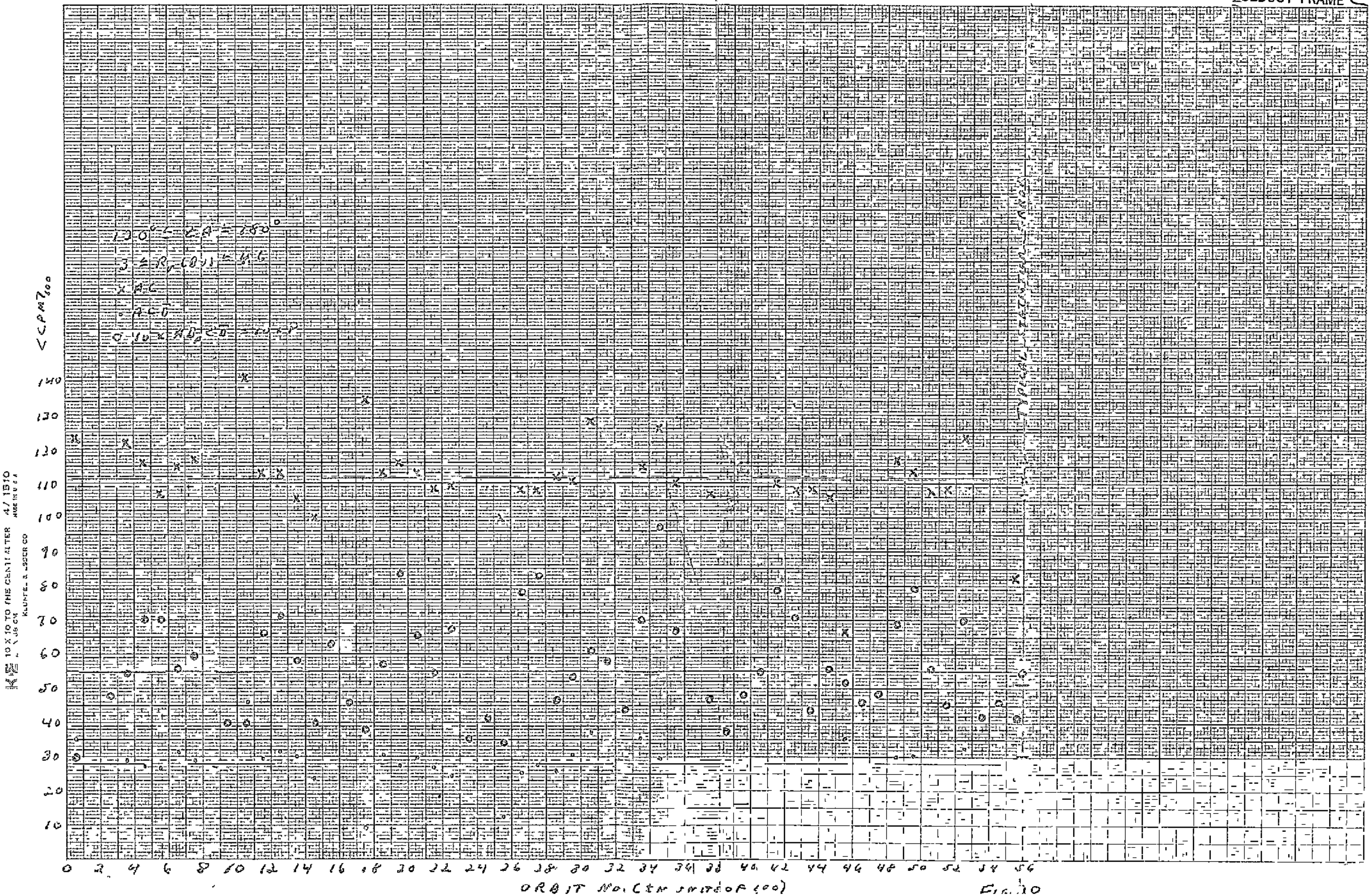

Fig. 10

FOLDOUT FRAME 1

FOLDOUT FRAME 2

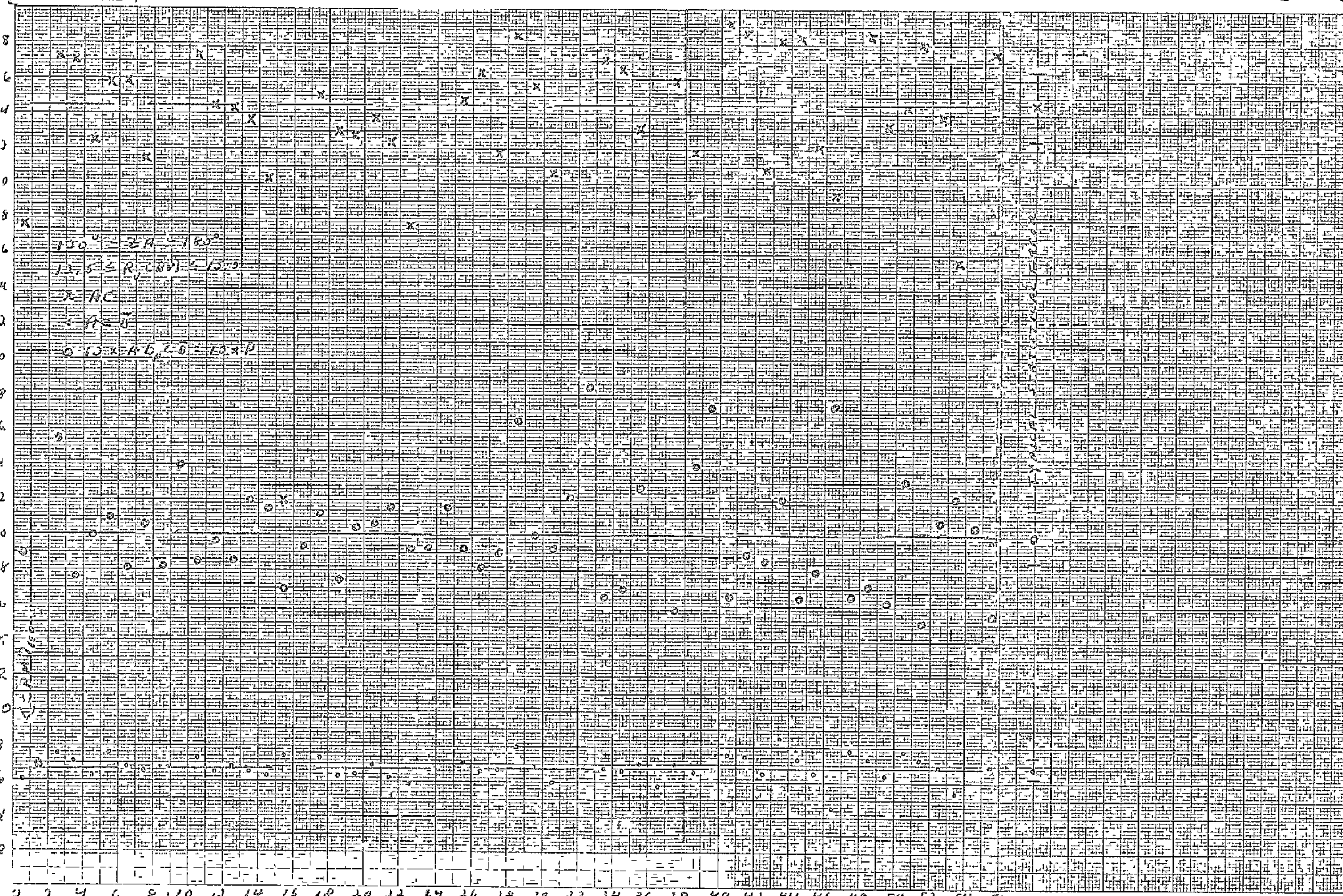

FIG. 21

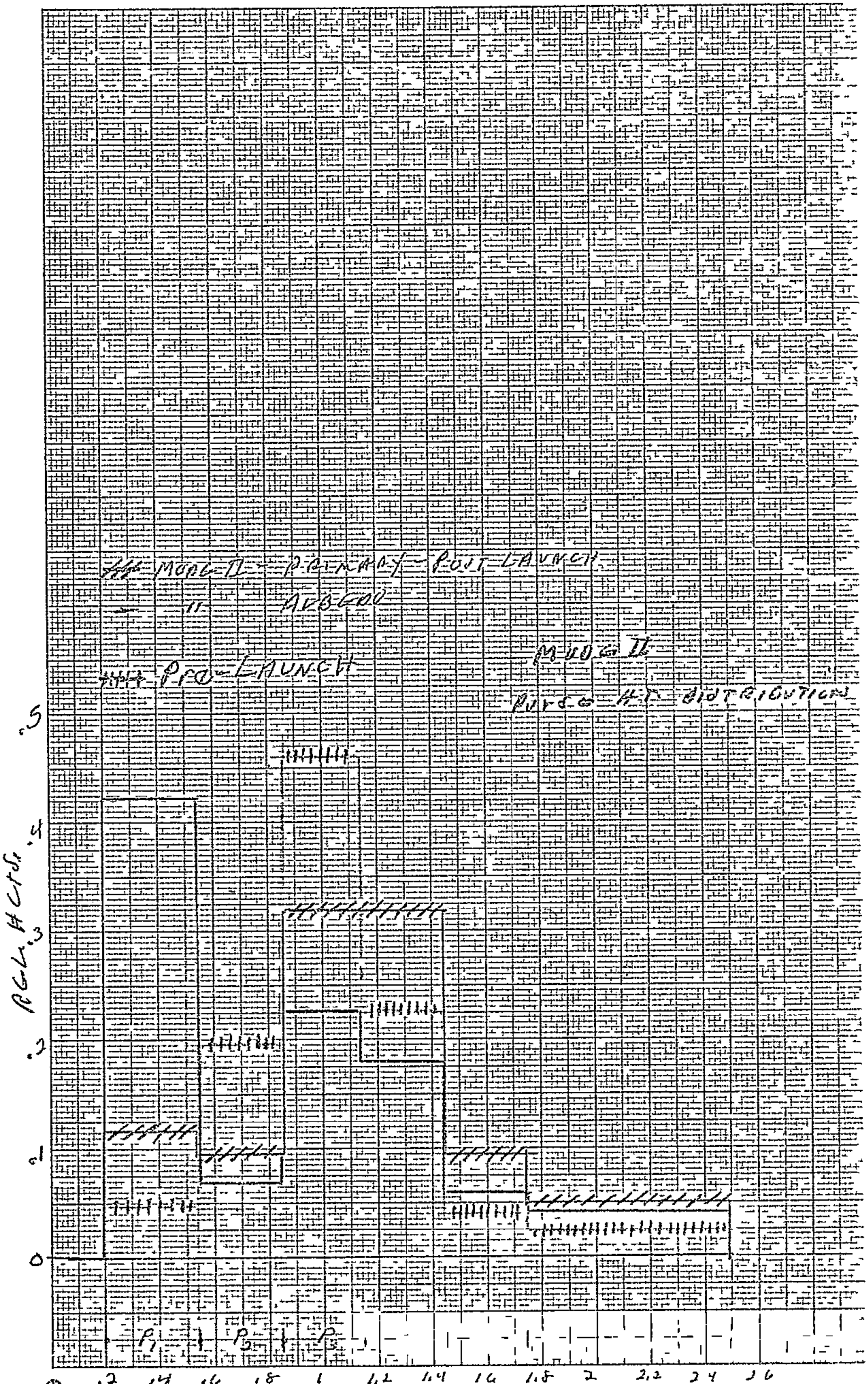
MODE II
PRE-LAUNCH
MODE II
.5
.4
.3
.2
.1
0
P1
P2
P3
0
.2
.4
.6
.8
1
1.2
1.4
1.6
1.8
2
2.2
2.4
2.6

Fig. 22

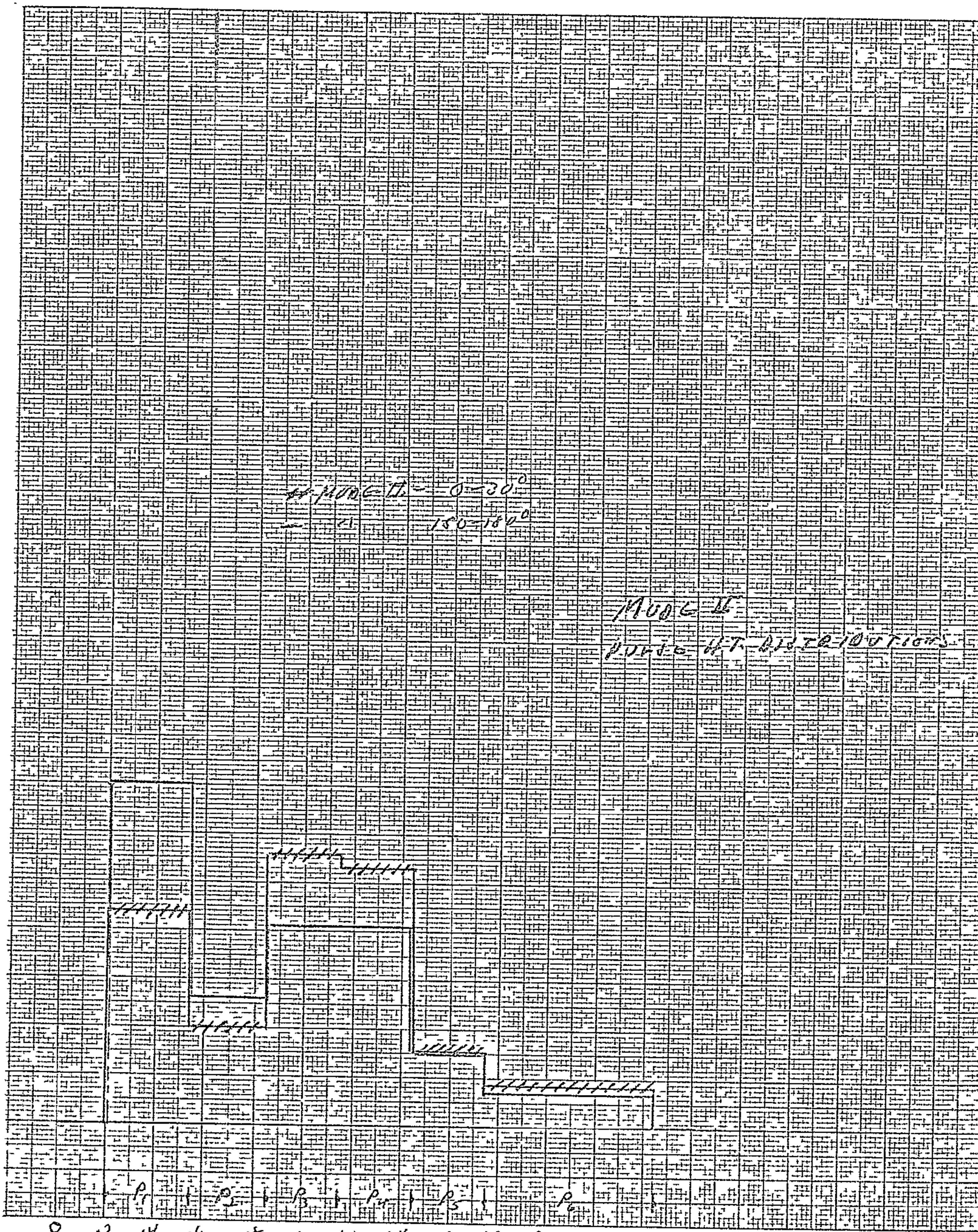
MODE II — 0–30°
150–180°
MODE II
PULSE HT. DISTRIBUTIONS
ρ1 ρ2 ρ3 ρ4 ρ5 ρ6
0 .2 .4 .6 .8 1 1.2 1.4 1.6 1.8 2 2.2 2.4 2.6

Fig. 23

VERTICAL C/O 4.3 - 5.2

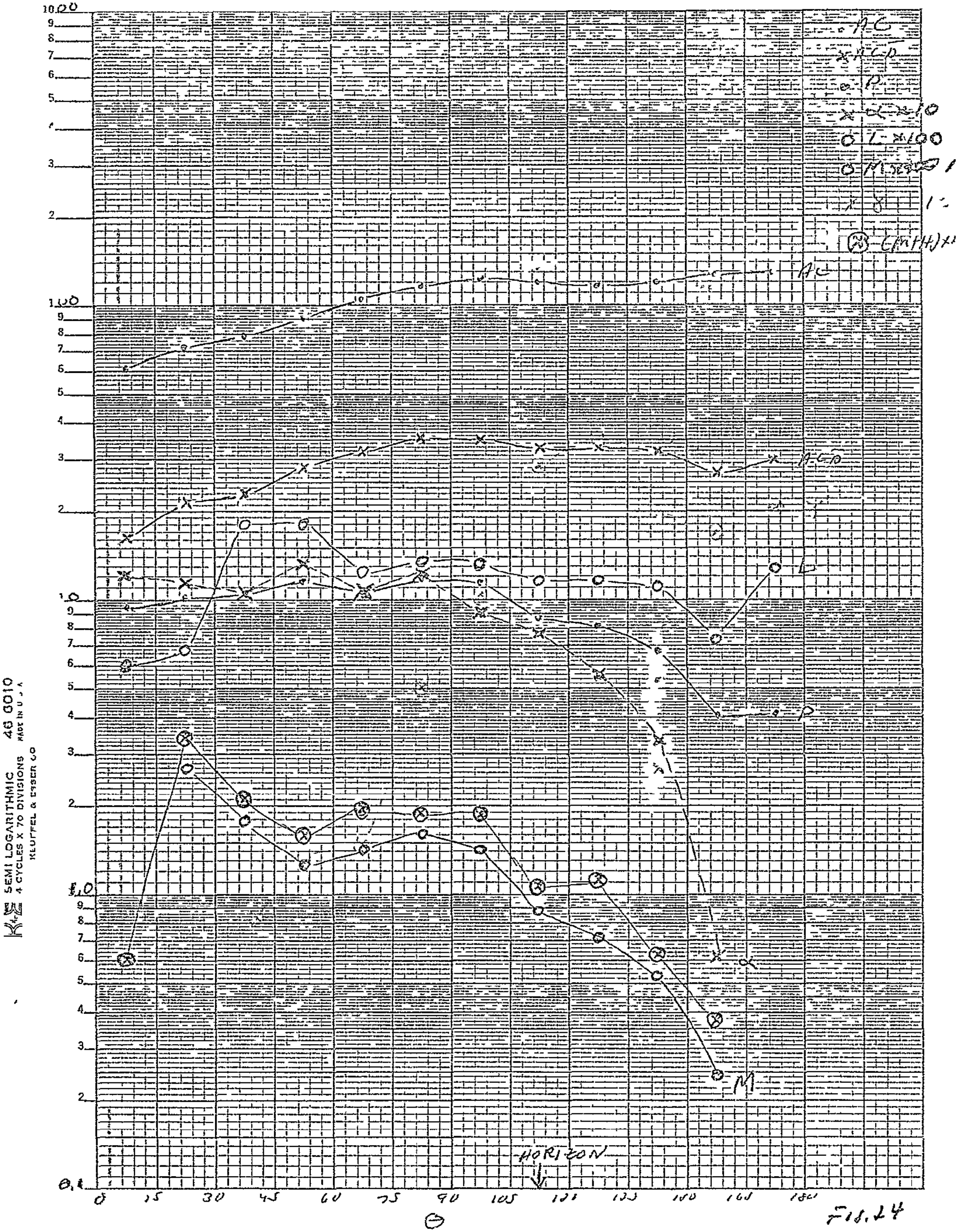

FIG. 24

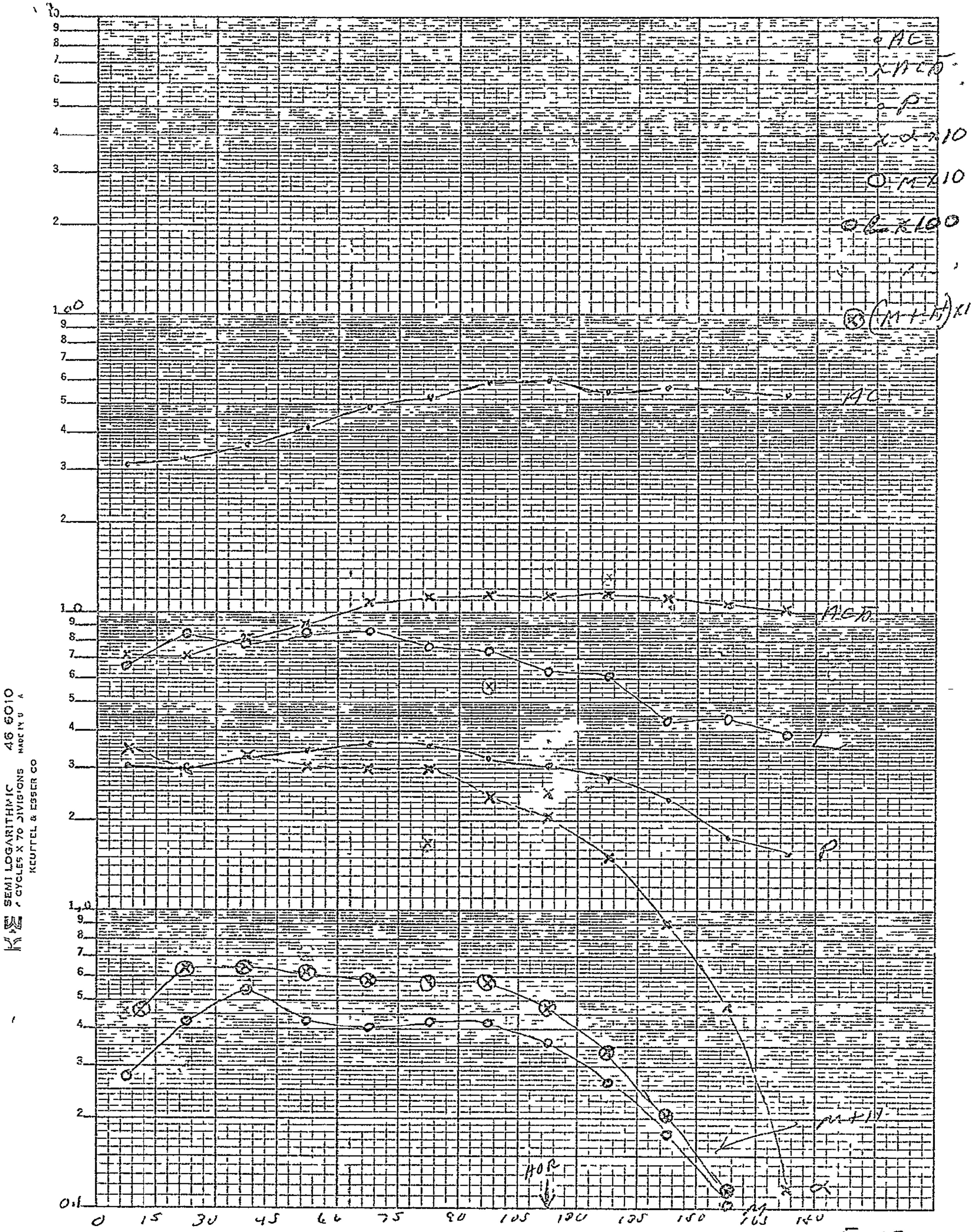
AC
AC/10
P
α×10
M×10
L×100
(M+H)×1
AC
AC/10
L
P
M+H
M
HOR
0 15 30 45 60 75 90 105 120 135 150 165 180
Θ
SEMI LOGARITHMIC 46 6010
KEUFFEL & ESSER CO

Fig. 45

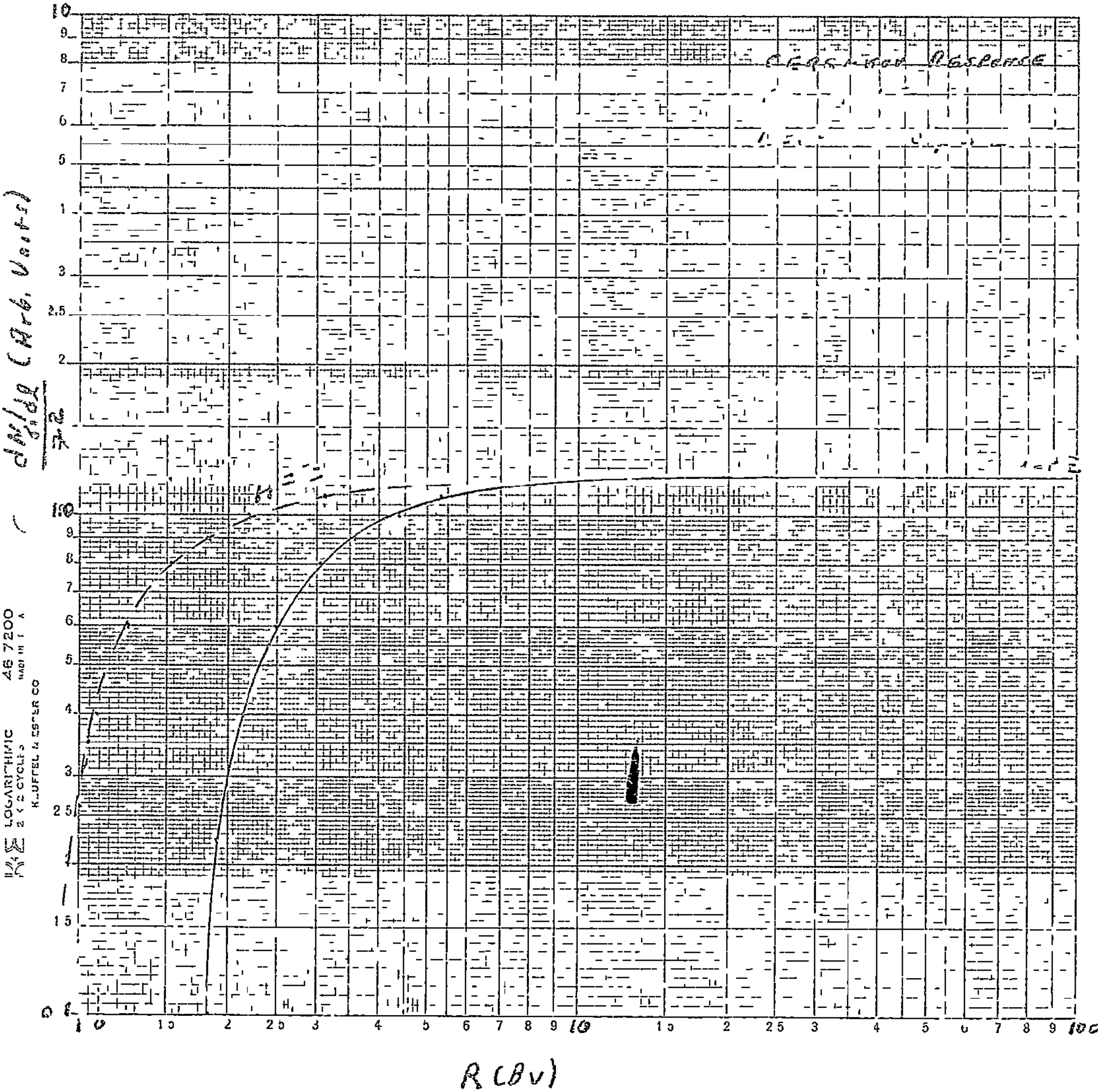

Fig. 26